# **PNAS**

1 2

> Youjun Zhang<sup>a,c,1</sup>, Yong Wang<sup>b,1</sup>, Yuqian Huang<sup>a</sup>, Junjie Wang<sup>b</sup>, Zhixin Liang<sup>b</sup>, Long Hao<sup>d</sup>, Zhipeng Gao<sup>d</sup>, Jun Li<sup>d,2</sup>, Qiang Wu<sup>d</sup>, Hong Zhang<sup>e</sup>, Yun Liu<sup>c</sup>, Jian Sun<sup>b,2</sup>, Jung-Fu Lin<sup>f,2</sup>

Collective motion in hcp-Fe at Earth's inner core conditions

7 8 9

3 4

5

6

- <sup>a</sup>Institute of Atomic and Molecular Physics, Sichuan University, Chengdu 610065, China.
- <sup>b</sup>National Laboratory of Solid State Microstructures, School of Physics and Collaborative Innovation Center 10
- of Advanced Microstructures, Nanjing University, Nanjing, 210093, China. 11
- <sup>c</sup>International Center for Planetary Science, College of Earth Sciences, Chengdu University of Technology, 12
- Chengdu 610059, China. 13
- <sup>d</sup>National Key Laboratory for Shock Wave and Detonation Physics, Institute of Fluid Physics, Mianyang 14
- 15 621900, China.
- <sup>e</sup>College of Physics, Sichuan University, Chengdu 610065, China. 16
- <sup>f</sup>Department of Geological Sciences, Jackson School of Geosciences, The University of Texas at Austin, 17
- 18 Austin, TX 78712, USA.

19

- 20 <sup>1</sup>Y. Z. and Y.W. contributed equally to this work.
- <sup>2</sup>To whom correspondence may be addressed: afu@jsg.utexas.edu; jiansun@nju.edu.cn; lijun102@caep.cn; 21

22

- Author Contributions. Y.J.Z., J.F.L, and J.S. conceived the project. Y.J.Z., Y.Q.H, L.H., and J.L. carried 23
- out the shock experiments and analyzed the experimental data. Y.W., J.J.W., Z.X.L., and J.S. performed 24
- the theoretical simulations and analyzed the data. Y.J.Z., Y.W., J.S., and J.F.L. wrote the manuscript. All 25
- authors contributed to the discussion of the results and commented on the manuscript. 26
- 27 **Competing interests.** The authors declare no competing interests.
- 28 Classifications: physical sciences
- 29 Keywords: Earth's core, high pressure, machine learning molecular dynamics, premelting, collective
- 30
- This PDF file includes: 31
- 32 Main Text
- Figures 1 to 5 33

# **Abstract**

36

37

38

39

40

41

42

43

44

45

46

47

48

49

50

51

52

53

54

Earth's inner core is predominantly composed of solid iron (Fe) and displays intriguing properties such as strong shear softening and an ultrahigh Poisson's ratio. Insofar, physical mechanisms to explain these features coherently remain highly debated. Here we have studied longitudinal and shear wave velocities of hcp-Fe (hexagonal close-packed iron) at relevant pressure-temperature (P-T) conditions of the inner core using *in-situ* shock experiments and machine learning molecular dynamics simulations. Our results demonstrate that the shear wave velocity of hcp-Fe along the Hugoniot in the premelting condition, defined as  $T/T_m$  ( $T_m$ : melting temperature of iron) above 0.96, is significantly reduced by ~30% while Poisson's ratio jumps to approximately 0.44. Machine learning molecular dynamics simulations at 230-330 GPa indicate that collective motion with fast diffusive atomic migration occurs in premelting hcp-Fe primarily along [100] or [010] crystallographic direction, contributing to its elastic softening and enhanced Poisson's ratio. Our study reveals that hcp-Fe atoms can diffusively migrate to neighboring positions, forming openloop and close-loop clusters in the inner core conditions. Hcp-Fe with collective motion at the inner core conditions is thus not an ideal solid previously believed. The premelting hcp-Fe with collective motion behaves like an extremely soft solid with an ultralow shear modulus and an ultrahigh Poisson's ratio that are consistent with seismic observations of the region. Our findings indicate that premelting hcp-Fe with fast diffusive motion represents the underlying physical mechanism to help explain the unique seismic and geodynamic features of the inner core.

5556

57

58

59

60

61

62

63

64

65

66

# **Significance**

Earth's solid inner core exhibits intriguing characteristics such as an exceptionally low shear-wave velocity and an ultrahigh Poisson's ratio that significantly deviate from our understanding for normal solid metals. In this study, we have used high pressure-temperature experiments and machine learning calculations with extremely large supercells to examine the dynamics and sound velocities of iron at the extreme pressure-temperature conditions of the inner core. Our research results reveal a drastic reduction in shear wave velocity when hcp-Fe approaches the melting point induced by shock. Our advanced machine learning calculations show that iron atoms undergo collective motion with fast diffusion in the premelting regime, leading to the ultralow shear modulus and ultrahigh Poisson's ratio. These results are consistent with seismic observations and

- 67 geodynamics of the inner core. We thus propose that collective motion in hcp-Fe is the underlying
- 68 physical mechanism for the soft inner core very close to the melting curve of constituent iron alloy.

# Introduction

Seismology and mineral physics studies over the past century reveal that Earth's inner core is mainly made of solid iron (approximately 96 wt% iron) (1, 2). The inner core only accounts for less than 1% of the planet's total volume but plays a key role in its dynamics, thermal evolution, core convection, and habitability. Of particular example is its nucleation and light element release to provide thermochemical energy sources powering the geodynamo, the generation of the magnetic field, and subsequent geological processes (3-5). Recent seismological investigations from modern J wave (6) and preliminary reference Earth model (1) have shown that the inner core has a shear wave velocity 30-40% lower than expected from solid hcp-Fe alloy at similar pressure, while the compressional wave velocity is overall consistent with that of the constituent Fe alloy (7, 8). This indicates an ultralow shear modulus in the inner core, with a Poisson's ratio (v) as high as 0.44-0.45, analog to that of soft metals such as lead and thallium (9) and close to that of molten iron (v = 0.5). The Poisson's ratio of the inner core is much larger than that of hcp-Fe estimated at the core's pressure and room temperature ( $v = \sim 0.35$ ) (10, 11). These seismic observations, therefore, suggest the existence of an extremely soft solid iron alloy with low rigidity in the inner core (12). This raises the fundamental question about the main underlying physical mechanism responsible for the unique seismic and geodynamic features in the region. Understanding the atomistic dynamics and its influence on the longitudinal  $(V_p)$ , bulk  $(V_b)$ , and shear  $(V_s)$  sound velocities of iron at inner core conditions can greatly enhance our knowledge of the inner working of our planet (13-15).

Driven by the continuous cooling of the planet, the solidification of the inner core occurs when its adiabat intersects the melting curve of the constituent iron alloy at the inner-core boundary (ICB) (16). Using the melting curve of pure iron as a reference, the melting temperature  $(T_m)$  at the ICB is determined to be ~6200(300) K at 330 GPa by experiments (17-21) and theories (22, 23). Addition of~4 wt.% light element(s) in iron is expected to depress the melting temperature by several hundreds of K (24). According to an isentropic modeling, the temperature gradient across the inner core radius (r),  $dT_i/dr$ , is expected to be approximately -0.17 K/km (16). This suggests that the temperature increase is only 100-200 K from the ICB to the center across the radius of ~1200 km. As a result, the inner core adiabat is expected to be within the temperature regime  $T_i/T_m$  exceeding 0.95. As the temperature approaches  $T_m$ , a previous study has suggested that solid metals can commonly show premelting behaviors with collective motion and fast atomic diffusion (25). Some simulations have predicted that unusual elastic and rheological properties occur in several

metals like Cu, Al, Ta, and Ca at the premelting temperature (26-28). This raises the possibility that premelting iron at  $T/T_m$  above 0.95 and inner-core pressures can exhibit unique elastic and rheological characteristics manifested in the aforementioned seismic observations.

102

103

104

105

106

107

108

109

110

111

112

113

114

115

116

117

118

119

120

121

122

123

124

125

126

127

128

129

130

131

132

133

To date, several hypotheses have been proposed to explain the observed seismic features in the inner core (7, 29-32). A pioneering study on the elasticity calculations of hcp-Fe predicted a strong shear softening at high P-T prior to melting (30), suggesting that premelting hcp-Fe may exhibit distinct behavior from ideal hcp-Fe. However, the simulation was conducted using relatively short simulation time and small cell size under homogeneous melting with superheating effects (> 7500 K at the ICB pressure where iron is expected to be molten) (30). On the other hand, first-principles DFT calculations showed that the shear modulus of hcp-Fe decreases quasi-linearly with temperature at a given density and agrees with the seismology and free oscillation data for the inner core without the requirement of premelting behavior (33, 34). Numerous high P-T experiments and modeling studies on the strength and plastic deformation have suggested that hcp-Fe is rheologically weak with a low shear strength due to pressure-induced slip and creep and its shear strength could be reduced by the elevated temperature (35-39). However, these experiments were conducted at P-T conditions far below from those of the inner core. Furthermore, some highpressure experiments and molecular dynamic (MD) computations indicate that iron carbide (e.g., Fe<sub>7</sub>C<sub>3</sub> compound (31)) or iron-hydrogen superionic alloy (32, 40) can reduce the shear wave velocity of the inner core. However, it is still highly controversial whether C and/or H light elements exist in Earth's inner core (24). Bcc-Fe has also been proposed as a possible explanation for the origin of the low shear wave velocity in the inner core (41-43), but in situ x-ray diffraction (XRD) experiments did not observe its existence at the relevant P-T conditions (19, 20, 44). Possible presence of melt pockets in the inner core has been suggested as an explanation for the high Poisson's ratio (45), although the inner core growth models indicate that interstitial liquid would have been squeezed out during its complete solidification and compaction below the solidus (46). Insofar, these existing hypotheses could help address some aspects of the inner-core's unique properties, but a comprehensive physical model incorporating direct experimental elasticity data and theoretical simulations with large supercells remains lacking.

Iron is believed to be stable in the hcp structure under the inner core P-T conditions as revealed by both static (18, 44) and dynamic (19, 20) experiments. In previous elasticity studies of iron, several experimental investigations of the sound velocities and Poisson's ratio of hcp-Fe have been carried out (29, 47-49); however, some experiments were conducted at relatively low P-T

conditions (e.g., up to ~73 GPa and 1700 K (29); up to ~300 GPa at room temperature (50, 51)) or did not reach to the temperature prior to melting points (e.g., static (49) and shock (47, 48) experiments). In this study, we have performed direct shock-wave measurements and machine learning-enhanced simulations with supercell sizes of more than 10,000 atoms to investigate the  $V_p$ ,  $V_b$ , and  $V_s$  of compressed hcp-Fe near the premelting temperature at the core pressure. Our theoretical results suggest that collective atomic motion occurs in premelting hcp-Fe, causing a strong sound velocity softening and enhanced Poisson's ratio. The collective motion-induced elastic softening in hcp-Fe is proposed to be the underlying physics to explain the unique seismic features of the inner core, including its ultralow shear wave velocity, low rigidity, and ultrahigh Poisson's ratio.

# **Results and Discussion**

High P-T shock compression experiments were conducted on high purity polycrystalline iron (>99.98%) using hypervelocity reverse-impact technique in two-stage light-gas guns (see *Materials and Methods* and *SI Appendix* Fig. S1). Iron was shock-compressed to pressures ranging from 82-231 GPa and temperatures ranging from 1600-5220 K along its Hugoniot P-T curve, where the shock Hugoniot temperature has been well determined by both experiments and simulations (17, 19, 23, 52) (see *SI Appendix* Table S1 and Fig. S8). The most recent shock compression experiments coupled with *in situ* XRD indicate that the hcp-Fe should be the only phase present at pressures between 200 and 1000 GPa prior to melting (19, 20). In this work, we targeted a maximum single shock pressure just below the pressure at which shock-induced melting occurs ( $\sim$ 242 GPa) (19). Therefore, iron should be in the hcp structure at the present investigated P-T range. We then obtained the (Eulerian) sound velocities of hcp-Fe including  $V_p$ ,  $V_b$ , and  $V_s$  under shock compression by solving the relationship among time interval, wave speed, and distance (see *SI Appendix* Figs. S2-S4).

Analysis of the shock experimental results indicates that the  $V_p$  of hcp-Fe linearly increases with increasing shock pressure ( $P_H$ ) between 80-160 GPa (Fig. 1a). After further shock pressure increase, the rate of change in  $V_p$  with respect to  $P_H$  ( $dV_p/dP_H$ ) gradually decreases and eventually changes to a negative slope above ~206 GPa. Additionally, the  $V_b$  in shock-compressed iron shows a monotonous increase from 82 to 231 GPa. Our measured  $V_p$  are generally consistent with those of shock-compressed iron in Refs. (48, 53), while we did not observe a sharp discontinuity of  $V_p$  at 200-220 GPa as reported earlier that was explained as a solid-solid phase transition from hcp to

a new phase (47). Our  $V_p$  results at relatively low P-T conditions agree well with an earlier report (49) on hcp-Fe up to ~163 and 3000 K using inelastic x-ray scattering (IXS) in laser-heated diamond anvil cells (LH-DACs) (Fig. 1a). Both sets of results support the notion that the  $V_p$  of hcp-Fe exhibits a quasi-linear relationship with density in this P-T range (49). However, our results suggest that as the P-T conditions approach the region of shock-induced melting, the sound velocity of hcp-Fe has a nonlinear relation with density and does not follow the quasi-linear sound velocity-density relationship (see *SI Appendix* Fig. S9). Our measured  $V_s$  of iron under shock compression shows a gradual increase with pressure and density from ~80 to 160 GPa but stops to increase above 160 GPa. At shock pressures above 200 GPa, the  $V_s$  of iron displays a dramatical drop from 4.2 km/s to zero as iron melts along the Hugoniot (Fig. 1a and *SI Appendix* Fig. S9).

Under shock compression, both P-T is simultaneously elevated along the Hugoniot, which could affect the sound velocities of hcp-Fe in a different way. Previous experiments using a LH-DAC has shown that the  $V_p$  and  $V_s$  of hcp-Fe generally increases with pressure but decreases with temperature (29, 54). Therefore, we have further investigated the effect of the shock Hugoniot temperature  $(T_H)$  on the sound velocity of hcp-Fe using the recently developed optical pyrometry technique (17). These results show that  $T_H$  in hcp-Fe increases monotonously from approximately 1600 to 5220 K as pressure increases from 82 to 231 GPa (see SI Appendix Fig. S8). Based on a consensual melting curve of hcp-Fe (17-21), we calculated its ratio of shock Hugoniot temperature to the melting point,  $T_H/T_m$ , which gradually increases from 0.44 to 0.96 with shock pressure from 82-231 GPa (see SI Appendix Table S1). We note that the  $V_s$  stops to increase at shock pressures above approximately 160 GPa, where the  $T_H/T_m$  approaches ~0.74. At P-T conditions further up to ~230 GPa, with a solid Hugoniot temperature close to the melting point  $(T_H/T_m \sim 0.96)$ , the  $V_s$ values drastically drops by approximately 30% (Fig. 1a). Our shock results reveal that the  $V_s$  of hcp-Fe at  $T_H/T_m \sim 0.96$ -1.00, which we define as the premelting region, displays a strong temperature-dependent reduction. This dramatic drop in the measured  $V_s$  agrees with some previous theoretical predictions by ab initio molecular dynamics (AIMD) simulations (30), which shows a strong nonlinear elastic constant weakening in hcp-Fe just before melting.

Based on our measured  $V_p$ ,  $V_b$ , and  $V_s$  along the Hugoniot, the derived Poisson's ratio of iron increases from ~0.34 to 0.43 as shock pressure increases from ~82 GPa (1600 K) to 231 GPa (5220 K), as shown in Fig. 1b. At conditions below ~160 GPa and 3450 K (with  $T_H/T_m$  less than ~0.74), the Poisson's ratio appears to be comparable to that of hcp-Fe at high pressure and room temperature (~0.35), as observed in DAC experiments (10, 11) (Fig. 1b), suggesting that

temperature has only a minor effect at relatively low values of  $T_H/T_m$ . Furthermore, static high-pressure experiments demonstrate that the Poisson's ratio of iron does not significantly change with increasing pressure to the core's at room temperature (10, 11), indicating that the rise in shock-compressed iron up to 230 GPa should be mainly due to shock-induced high temperatures. When compared to seismic observations, the Poisson's ratio of 0.43 in hcp-Fe at  $T_H/T_m \sim 0.96$  and  $P_H \sim 230$  GPa is generally consistent with the ratio of  $\sim 0.44$ -0.45 in the inner core (the striped rectangle area in Fig. 1b).

To gain insight into the atomistic behavior and lattice dynamics of premelting hcp-Fe, we developed a machine learning potential with density-functional-theory (DFT) accuracy, using the deep concurrent learning method (see Materials and Methods and SI Appendix Figs. S5-S7). Equilibrium and non-equilibrium molecular dynamics simulations (EMD and NEMD) were conducted at pressures ranging from 230-330 GPa and at various temperatures, up to the nanosecond simulation scale. At temperatures close to the melting point  $(T/T_m > \sim 0.96)$ , we observed the spontaneous emergence of atomic collective motion in hcp-Fe, along its [100] or [010] crystallographic orientation, where Fe atoms diffuse collectively in both intralayer and interlayer directions (Fig. 2a and SI Appendix Movie S1). Specifically, most atoms exhibit a onedimensional (1-D), longitudinal wave-like behavior in open-loop (chain-like) diffusions, wherein one atom jumps out of its equilibrium position and pushes its neighboring atoms along specific crystallographic directions, such as [100] or [010] in the a-b plane (Fig. 2b). This collective motion generates a wavefront of diffusion, moving randomly forward until it meets a vacancy and releases the compression. This phenomenon was detailed proposed in cubic Ca within the premelting regime under high pressure and has been indicated as a possibly prevalent high-temperature feature in metals under extreme conditions (28). The longitudinal-wave-like behavior could dissipate shear in the system at the atomistic level, which was also observed in the premelting bcc-Ta (55) and fcc-Al (56) at ambient pressure.

The distribution of iron atomic displacements is also investigated within a given lag time (up to 0.1 ns) using time-dependent van Hove self-correlation functions  $P(\Delta r, t)$  (57, 58). At the Vs softening regime (e.g.,  $T/T_m \sim 0.98$ ), hcp-Fe atoms migrate collectively to their neighboring lattice points. This migration leads to a non-Gaussian multiple-peak distribution of  $P(\Delta r, t)$  (horizonal dashed-line in Fig. 2c). However, in solid hcp-Fe at a relatively low temperature below the region (e.g.,  $T/T_m \sim 0.92$ ),  $P(\Delta r, t)$  exhibits a stable Gaussian distribution over time in the nanosecond-scale simulation, indicating the absence of collective motion (see *SI Appendix* Fig. S11).

Furthermore, we computed the mean square displacements (MSD) for hcp-Fe at different temperatures and found that the MSD of premelting hcp-Fe at 230 GPa and 5300 K ( $T/T_m \sim 0.98$ ) steadily increases throughout 250 picosecond (ps) simulation time. This means that collective motion contributes to significant diffusion of atoms (Fig. 3a). Notably, the average diffusion in the a-b planes of premelting hcp-Fe spreads faster than that along the c-axis. Conversely, at a relatively low temperature of 4000 K ( $T/T_m \sim 0.74$ ) at 230 GPa, the MSD of hcp-Fe atoms remains nearly constant during the simulation time, indicating no observable diffusion (Fig. 3a).

For a deeper understanding of the collective atomic motion in premelting hcp-Fe, we have theoretically investigated its finite-temperature phonon dispersions including the anharmonicity and enthalpy at 230 GPa and various temperatures (Fig. 3b). Our calculations show abnormal softening in some high symmetry points at high P-T (Fig. 3b), corresponding to the relative vibrations between close-packed planes along the c-axis in hcp structures (Fig. 3c). These softening reflect temperature effects as a dynamical driving force for collective atomic motion, which mostly diffuses between the close-packed planes of hcp-Fe. From an energetic perspective, the mixture of solid and liquid near melting promotes disorders and increases the system's potential energy compared to an ideal hcp-Fe crystal. However, the directional priority of collective motion pushes atoms to diffuse along the lowest energy paths, which only slightly increases the system's enthalpy compared to ideal hcp-Fe without collective motion (Fig. 3d). Given the complexity of the potential energy surface at high temperatures and the large entropy induced by the collective motion, hcp-Fe with collective motion may be dynamically stable in the premelting P-T conditions.

To investigate how collective atomic motion affects physical properties of hcp-Fe, we conducted calculations on its elastic constants and Poisson's ratio at high P-T. It should be noted that traditional elastic modulus calculations using EMD method for single crystal hcp-Fe are susceptible to superheating effects. To overcome this, we employed a solid defective structure quenched from the two-phase model in NEMD simulations to mitigate the impact of superheating in order to accurately calculate the high P-T elastic constants (see Supplementary Material). Results from both the *ab initio* method and the constructed machine learning model show that a significant shear elastic softening occurs in hcp-Fe at 230 GPa as the temperature approaches the melting point, consistent with the present experimental observations (Fig. 4). The present calculations and experiments indicate that the shear modulus of hcp-Fe at 230 GPa and  $T/T_m \sim 0.96-0.98$  agrees overall with the seismically observed low shear modulus of the inner core (Fig.

4). Furthermore, the calculated Poisson's ratio using NEMD increases from 0.36 to 0.42 as the temperature rises from 300 to 5000 K ( $T/T_m \sim 0.92$ ) at 230 GPa (Fig. 1b). When the temperature continues to rise from 5000 K to the melting point at 5400 K, the Poisson's ratio of hcp-Fe increases dramatically from 0.42 to 0.5. Our computations reveal that the Poisson's ratio in hcp-Fe with collective motion is approximately 0.45 at 230 GPa and 5200 K ( $T/T_m \sim 0.96$ ), which is overall consistent with our experimental value at similar P-T conditions (Fig. 1b).

We conducted more calculations at pressures ranging from 230 to 330 GPa and temperatures between 4000 and 7000 K to determine the P-T regime of hcp-Fe with collective motion at relevant inner core conditions. Our results reveal the dynamic phase boundary between ideal hcp-Fe and hcp-Fe with collective motion, as well as the boundary between hcp-Fe and liquid Fe (Fig. 5). We found that the temperature for hcp-Fe with collective motion ( $T_c$ ) extends approximately 500 K below its  $T_m$  at inner core pressures. Comparison between our predicted dynamic phase of hcp-Fe with collective motion and a typical adiabat of iron core indicates that the inner core adiabat is slightly below the  $T_m$  and falls within the temperature region of premelting hcp-Fe with collective motion (Fig. 5 and SI Appendix Fig. S13). As mentioned in the Introduction, the  $T/T_m$  of the inner core is expected to be between 0.95-0.99 (16, 59). Our results indicate that the dynamics of collective motion in the premelting hcp-Fe at the conditions relevant to the inner core may be the primary physical mechanism behind the observed seismic properties, such as the ultralow shear wave velocity, low rigidity, and ultrahigh Poisson's ratio (6).

Earth's inner core also contains ~5 wt.% Ni and ~4 wt.% light element(s) alloyed with iron, though the exact identity of the major light element remains uncertain (24). Here we consider Si as a candidate light element as an example to understand light element effects on  $T_m$  depression and associated elasticity. Addition of 4 wt.% of Si in Fe or Fe-Ni alloy would lower the melting temperature to a  $T_m$  of ~5800 K (60) and overall increase the  $V_p$  by 3-5% (50, 54, 61, 62). Meanwhile, Fe alloyed with ~5 wt.% Ni and a few % of Si would retain the hcp structure at relevant inner-core P-T conditions (63-65). Using a temperature gradient of 100-200 K in the inner core, we estimated that the expected inner core adiabat for iron alloyed with a few wt.% light elements would have a  $T/T_m$  of ~0.97-0.98, which falls within the premelting region ( $Tc/T_m$  > ~0.95). These results suggest that such an Fe-Ni-light element alloy can also exhibit collective atomic motion, resulting in the ultralow shear wave velocity and ultrahigh Poisson's ratio of the inner core.

Our research into the effects of collective atomic motion on premelting hcp-Fe has yielded exciting results regarding its shear softening and ultrahigh Poisson's ratio. These findings provide

a novel physical mechanism to explain the unique seismic and geodynamic features of Earth's solid inner core. The ultralow shear modulus in premelting hcp-Fe suggests that the inner core may have relatively low shear viscosity, making it susceptible to deformation and convectively instability (66). Future exploration into the atomistic dynamic behavior and high pressure-temperature sound velocities of iron alloyed with approximately 5 wt.% nickel and 2-4 wt.% light elements at the inner-core conditions is necessary to shed more light on the geophysics and geodynamics of both the inner and outer cores. Together with previous research on premelting metals (26-28), a scenario beyond the perspective of classical nucleation theory together with its potential effects on material properties such as the elasticity need to be further clarified in future works.

#### Figures and captions:

305

306

307308

309

310

311

312

313

314

315

316

317

318319

320321

322

323

324

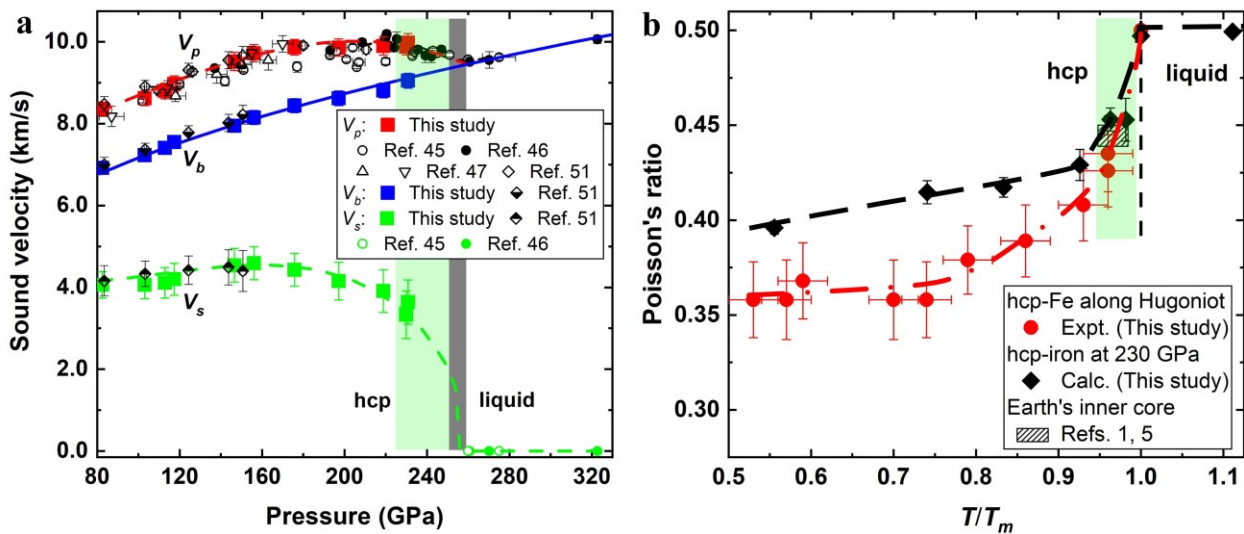


Fig. 1. Sound velocities and Poisson's ratio of iron along the shock Hugoniot conditions. (a) Measured sound velocities  $V_p$  (red squares),  $V_b$  (blue squares), and  $V_s$  (green squares) of iron under shock compression. Solid (48) and open (47) circles are the measured  $V_p$  under shock compression from the literature results. Diamonds, diamonds with bottom half black, and diamonds with top half black represent the measured  $V_{\nu}$ ,  $V_b$ , and  $V_s$ , respectively, under shock compression by Ref. (53). The triangles and inverted triangles represent the measured  $V_p$  of hcp-Fe at given pressures and ~3000 and 2300 K, respectively, using IXS in LH-DACs (49). The blue line represents the calculated  $V_b$  of iron using a thermodynamic equation under shock compression. The red dashed line in  $V_p$  was fitted to the measured data using a third-order polynomial and is meant as a guide for the eye. The green dashed line through the experimental data in  $V_s$  are derived from the  $V_p$  and  $V_b$ . The vertical grey bar represents the pressure range for iron melting to occur along the shock Hugoniot. (b) Measured and calculated Poisson's ratio of hcp-Fe as a function of the ratio of temperature to the melting point of iron  $(T/T_m)$ . By definition, the Poisson's ratio reaches 0.5 at  $T/T_m$  of 1.0 in molten iron (horizontal dashed black line). The Poisson's ratio of the inner core constrained by seismic observations falls within the range of 0.44-0.45 (striped rectangle region) (1, 6), which is located at  $T/T_m \sim$ 0.96 for hcp-Fe at high pressure. The difference in Poisson's ratio between experimental and computational results at relatively low  $T/T_m$  may be attributed to the pressure difference between Hugoniot conditions in experiments and isobaric conditions in calculations. The light-green region indicates a significant shear softening and ultrahigh Poisson's ratio induced by collective atomic motion in hcp-Fe at shock pressures above ~230 GPa and  $T/T_m$  greater than ~0.96.

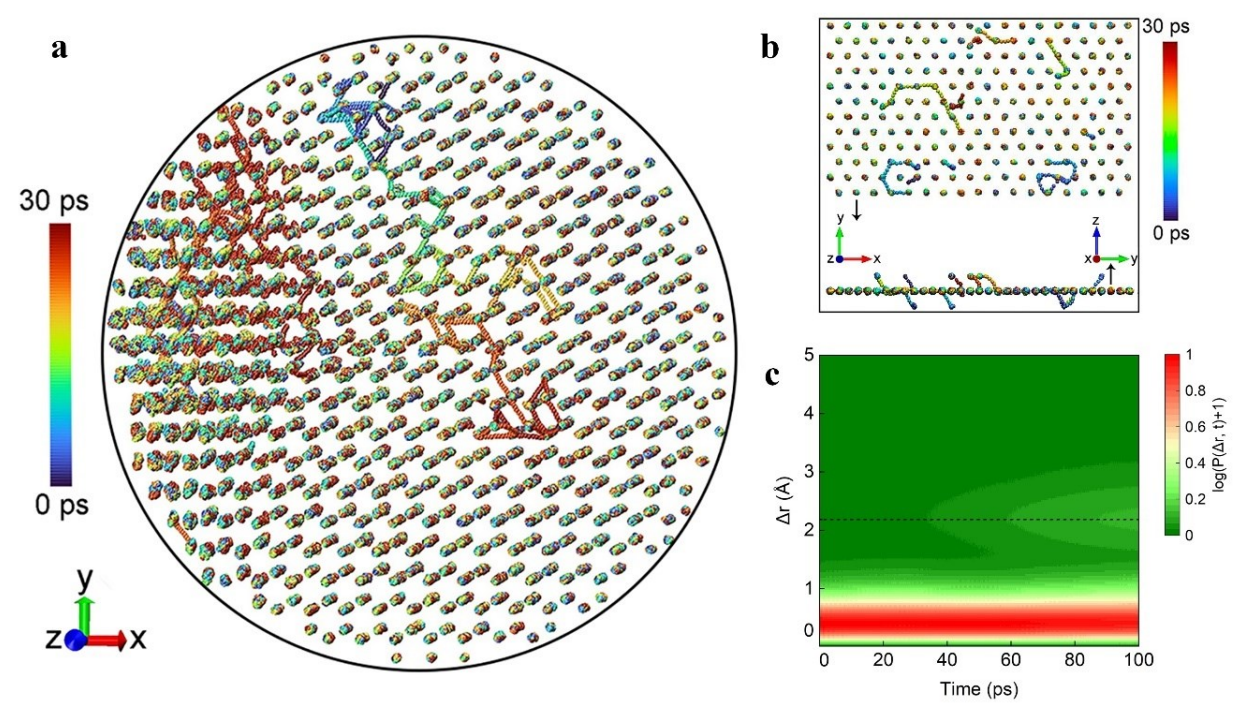
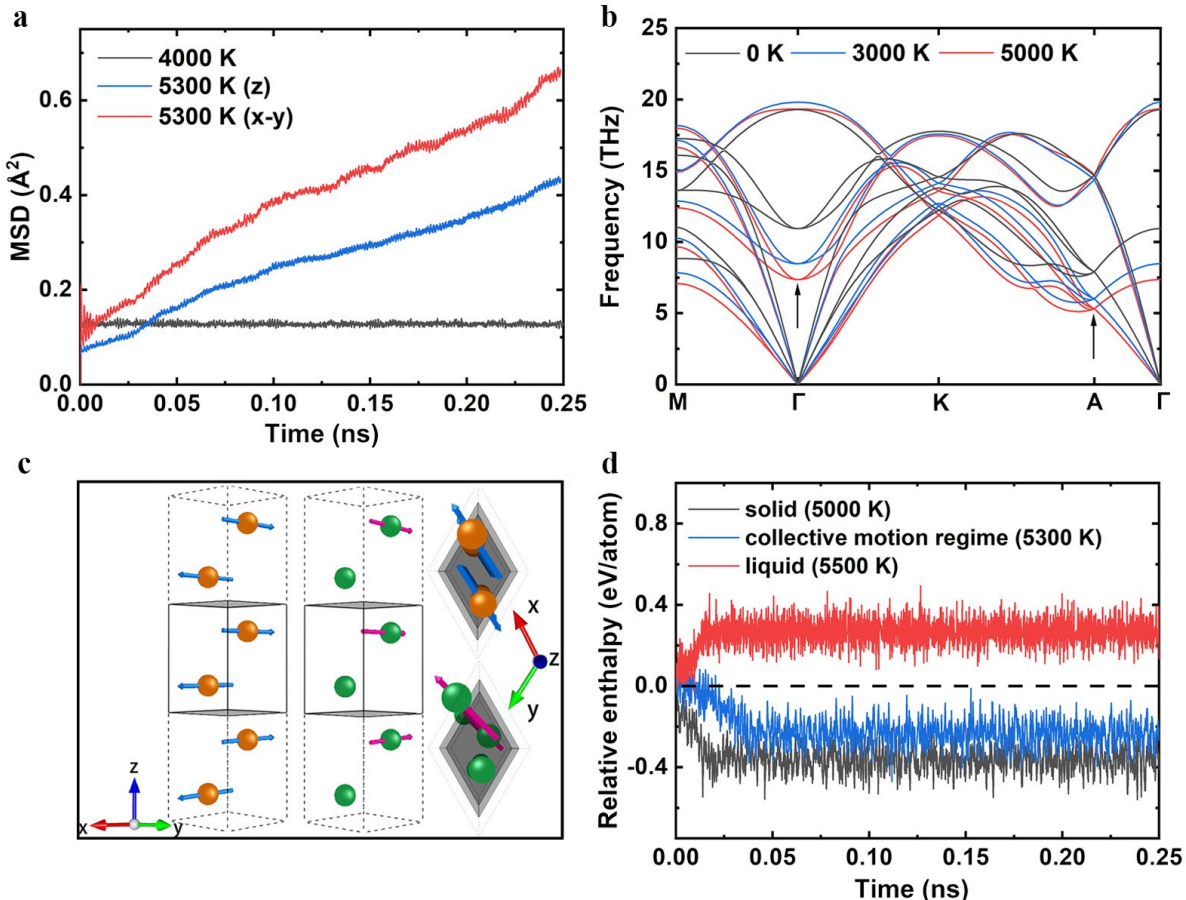


Fig. 2. Collective atomic motion of compressed hcp-Fe at near melting point and 230 GPa. (a) Dynamic behavior of hcp-Fe atoms at 230 GPa and near melting temperature ( $T/T_m \sim 0.98$ ) using machine learning molecular dynamics. Iron atoms are colored with time over a 30 picosecond (ps) period in the snapshot. (b) Top- and side-view dynamical snapshots of a single close-packed a-b (x-y) plane during 30 ps in premelting hcp-Fe with collective motion. Iron atoms predominantly diffuse along [100] or [010] directions of the hcp structure. This diffusion leads to the formation of open-loop strings and a few closed-loop shapes such as triangular. The open-loop diffusion behavior propels iron atoms to form a 1-D longitudinal wave-like pattern. Snapshots in (a) and (b) were smoothed within a 1 ps time window to eliminate thermal noises. (c) Self van Hove correlation function  $P(\Delta r, t)$  of premelting hcp-Fe. Iron atoms migrate to neighbors during collective atomic motion, which induces multiple-peak non-Gaussian distribution vs. time in the correlation functions. The  $P(\Delta r, t)$  represents the probability of finding an atom at distance  $\Delta r$  after a time interval t. Vertical bar represents the logarithm form of the  $P(\Delta r, t)$  to highlight the diffusion of collective motion (marked by the black dashed line as the nearest neighbor distance).



341342

343

344

345

346347

348

349

350

351

352

353354

355356

Fig. 3. Dynamical properties of hcp-Fe at ~230 GPa and representative temperatures. (a) Calculated mean square displacements (MSD) of hcp-Fe atoms at 230 GPa and varied temperatures. The atoms in premelting hcp-Fe diffuses with the simulation time. The diffusion of hcp-Fe atoms primarily occurs in the a-b planes as they migrate to neighboring atoms. Diffusion in the z-direction is usually triggered by the vacancies' migration between different a-b planes, of which vacancies were made by the collective motion in a-b planes. (b) Phonon spectra of hcp-Fe at 230 GPa and three given temperatures (0 K, 3000 K, and 5000 K). Anharmonicity is taken into consideration in the calculations. Black arrows highlight some modes in the phonon spectra that show strong softening as the temperature increases. (c) Schematic diagram of the softening direction of hcp-Fe at high P-T. Blue arrows through orange atoms show a strong phonon softening in the Γ point of hcp-Fe reduced from ~12 THz at 0 K to ~7 THz at 5000 K and at 230 GPa, where the vibrational direction is between adjacent a-b close-packed planes. Magenta arrows through green atoms show a similar softening direction in the A (0, 0, 0.5) point, where the softening happens between nonadjacent planes. (d) Enthalpy of iron in hcp, hcp with collective motion, and liquid states, respectively, at 230 GPa as a function of simulation time. Systems evolve from the initial solid-liquid mixture to hcp crystal at 5000 K ( $T/T_m \sim 0.92$ ), to hcp with collective motion at 5300 K ( $T/T_m \sim 0.98$ ), and to liquid at 5500 K ( $T/T_m$  $\sim 1.02$ ), respectively. The horizontal dashed line represents the initial enthalpy of the solid-liquid mixture (see SI Appendix Fig. S7).

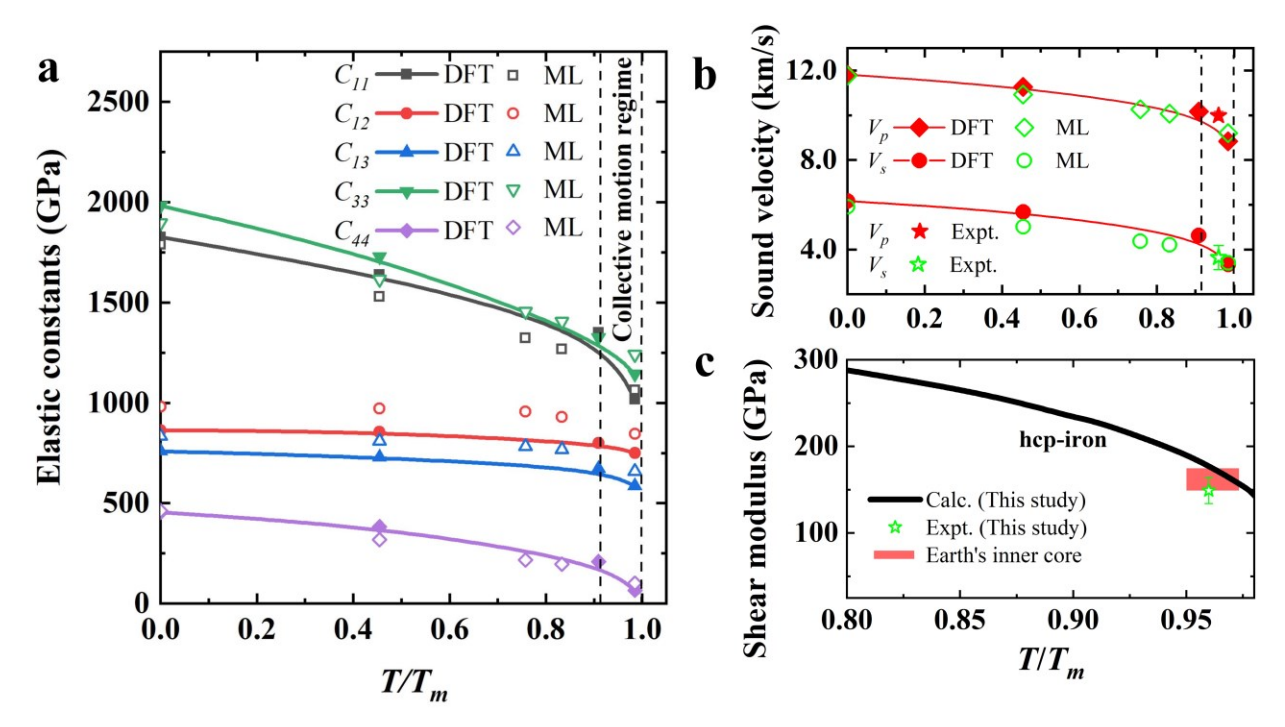


Fig. 4. Elastic constants, sound velocities, and shear modulus of hcp-Fe at high pressure-temperature conditions. (a) Calculated clastic constants of hcp-Fe as a function of the ratio of temperature to its melting point  $(T/T_m)$  at 230 GPa. The elastic constants were calculated using both the DFT-AIMD and machine learning (ML) method. (b) Comparisons of sound velocities of hcp-Fe between theoretical and experimental results at high temperatures and 230 GPa. Solid and open symbols represent the results from the DFT-AIMD and ML calculations, respectively, in this study. The melting point  $T_m$  of iron at 230 GPa is calculated to be ~5400 K by two-phase methods (see *SI Appendix* Fig. S8). The region between vertical dashed lines covers the premelting condition. The calculated longitudinal and shear wave velocities are consistent with our experimental results at ~230 GPa and  $T/T_m \sim 0.96$ . The shear softening emerges near melting, which accompanies by collective motion in the large spatiotemporal machine learning molecular dynamics (See *SI Appendix* Movie S1). (c) Calculated (black curve) and measured (open star) shear modulus of hcp-Fe at high temperatures and 230 GPa. The shear modulus of premelting hcp-Fe at the relevant conditions of the core can overall match with the seismic observation of 149-176 GPa (red region) in the inner core (red bar) (1, 6).

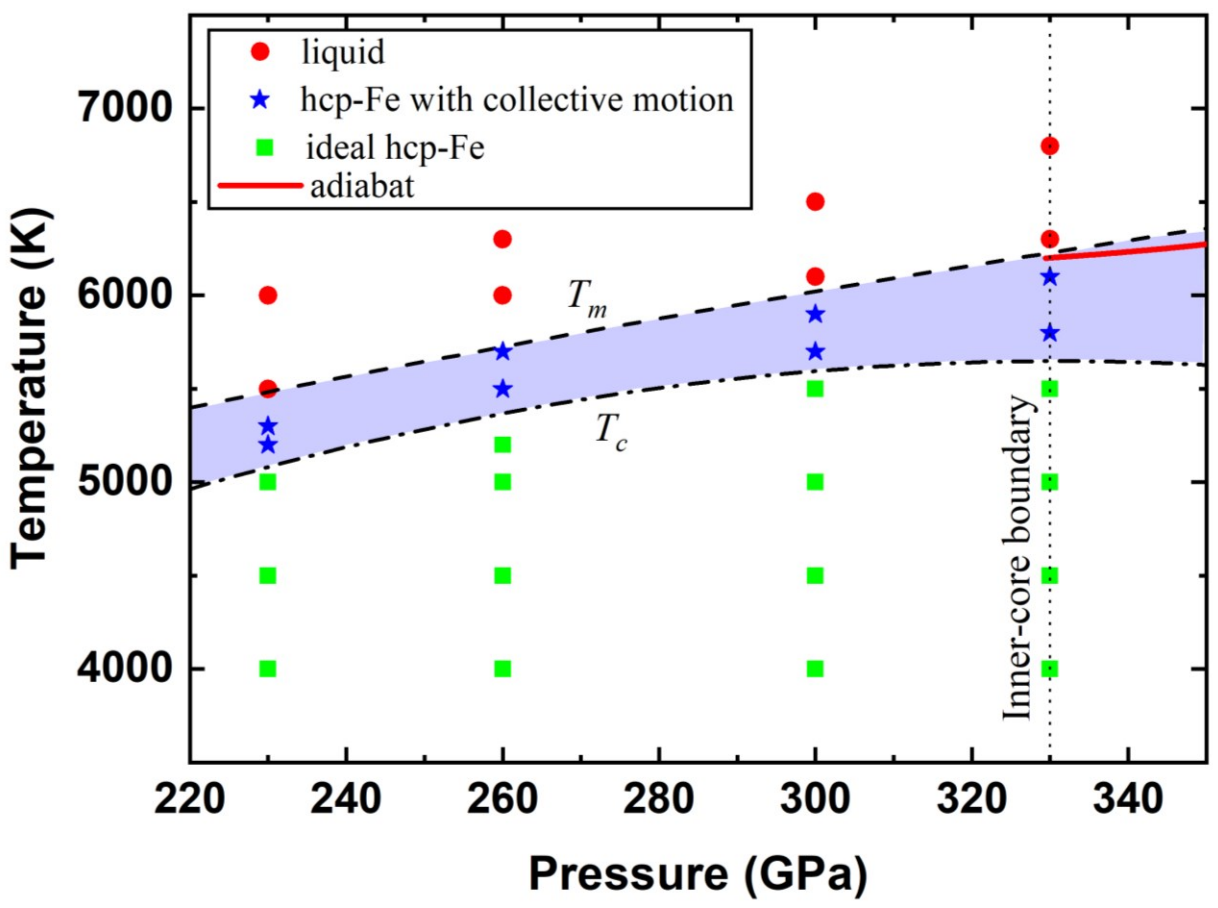


Fig. 5. Predicted dynamic phase boundary of hcp-Fe with collective atomic motion at high pressure-temperature conditions relevant to the Earth's core. The dashed line represents the melting curve  $(T_m)$  of iron at high pressures in this study fitted by Simon-Glatzel law with  $T_m = T_0 (P/11.8+1)^{0.367}$ , where  $T_0 = 1811 \text{ K}$  is the melting point of iron at ambient pressure. Our calculated melting points of iron is generally consistent with recent experimental results as shown in *SI Appendix* Fig. S8 (17-21), in which the melting point is ~6200 K at the pressure of the inner-core boundary (~330 GPa). The dash-dotted line represents the dynamic phase boundary between ideal hcp-Fe and hcp-Fe with collective motion  $(T_c)$  in this study fitted by a second-order polynomial. The light-blue area represents the predicted P-T conditions of hcp-Fe with collective motion. The red curve represents a typical adiabat of iron anchored at the inner core boundary. The adiabat gradient across the inner-core boundary is approximately 0.17 K/km based on isentropic modeling (16).

#### **Materials and Methods**

Starting Materials. High-purity polycrystalline bulk iron with a purity greater than 99.98% was used as the starting material. The iron sample were prepared into 0.662-1.480-mm-thick disks with a diameter of ~24 mm, and their surfaces were polished to a mirror finish with a roughness of ~15 nm (17).

Sound velocity measurements and Poisson's ratio of hcp-Fe at high P-T. Reverse-impact experiments (see SI Appendix Fig. S1) were carried out at both Sichuan University and Institute of Fluid Physics in China. We employed both lithium fluoride (LiF) crystal with <100> orientation and sapphire Al<sub>2</sub>O<sub>3</sub> crystal with <0001> orientation as window materials, respectively. The interface particle velocity profile was measured using photon Dopler velocimetry (PDV) with a laser wavelength of 1550 nm and a time resolution of less than 1 nanosecond. The impact velocity was measured using an electromagnetic method with an uncertainty of ~0.5%. In the first series of runs, we used LiF crystals with <100> orientation as the transparent window, where the particle velocity profile was recorded at the sample/window interface. This allowed us to generate P-T conditions up to ~156 GPa and ~3400 K with the highest impact velocity being 7.472(37) km/s. To achieve higher pressures, we employed Al<sub>2</sub>O<sub>3</sub> crystals with <0001> orientation as the window material in the second series of runs because it is denser than LiF crystal and can generate much higher P-T on reverse impact. Even after the phase transformation to CaIrO<sub>3</sub>, Al<sub>2</sub>O<sub>3</sub> crystal remained transparent up to at least 210 GPa, and its refractive index under shock compression was recently determined (67). Iron was shocked to Al<sub>2</sub>O<sub>3</sub> crystal up to the impact velocity of 7.695(30) km/s, reaching in the highest P-T of ~230.8 GPa and ~5220 K in this study. The particle velocity wave profiles for these shots are shown in SI Appendix Fig. S2.

To ensure experimental accuracy, we used four PDV probes to simultaneously measure the particle velocity profiles at four different locations of the sample in a shot (see *SI Appendix* Fig. S3): one probe was positioned at the center of the impact surface, while the other three were located at the outer ring with a diameter of 5 mm. The wave profiles recorded by multiple probes almost overlapped in one shot, indicating low uncertainty in the sound velocity measurements (< 3%). The Lagrangian longitudinal sound velocity of iron,  $C_l$ , can be directly obtained using the measured time interval ( $\Delta t$ ) and the thickness of the sample ( $\delta$ ):

$$C_l = \frac{\delta}{(t_1 - t_0) - \delta/U_s} = \frac{\delta}{\Delta t - \delta/U_s} \tag{1}$$

Then, the Eulerian longitudinal sound velocity,  $V_p$ , which accounts for the change of sample thickness due to shock compression (68), is:

417 
$$V_p = \frac{\rho_0}{\rho_H} C_l = \frac{\rho_0}{\rho_H} \frac{\delta}{(t_1 - t_0) - \delta/U_S}$$
 (2)

where  $\rho_0$  and  $\rho_H$  are the starting and compressed densities of iron,  $U_s$  represents the shock wave velocity in shock-compressed iron. The time interval is represented by  $\Delta t = t_2 - t_1$ .  $t_1$  and  $t_2$  is the time of impact and the arrival of the release wave at the impact interface, respectively, which can be obtained from the measured interface particle velocity profile (see *SI Appendix* Figs. S2-S3). The Lagrangian bulk sound velocity ( $C_b$ ) at the Hugoniot state can be determined by linearly extrapolating the plastic unloading part of the  $C_l$  line to the Hugoniot state (see *SI Appendix* Fig. S4). The elastic-plastic transition point at time  $t_2$  can be identified by calculating the derivative of particle velocity with respect to time (see *SI Appendix* Fig. S3). The Eulerian bulk sound velocity  $V_b$  is obtained by substituting  $t_1$  with  $t_2$  in equation (2) (53). By using  $V_p$  and  $V_b$ , the shear wave velocity,  $V_s$ , can be obtained using the following relation:

$$V_s^2 = \frac{3}{4} (V_p^2 - V_b^2) \tag{3}$$

433

437

439

440

441

443

444

446 447

450

451

452 453

454

455

456 457

458

459 460

461

The reverse-impact experiments (69-71) do not require the fitting of the overtake ratio of sample plate 428 thickness to impactor plate thickness, which differs from symmetric impact experiments previously used 429 430 (47, 48). Instead, this method directly measures the shock and rarefaction fronts in iron samples, which 431 leads to a significant improvement in the accuracy of sound velocity measurements.

On the other hand, the bulk sound velocity  $(V_b)$  of iron under shock compression can be calculated using a thermodynamic equation:

434 
$$V_b^2 = -V^2 \frac{dP_H}{dV} \left[ 1 - \left( \frac{\gamma}{V} \right) \frac{(V_0 - V)}{2} \right] + V^2 \left( \frac{\gamma}{V} \right) \frac{P_H}{2}$$
 (4)

435 
$$P_H = \rho_0 C_0^2 (1 - \rho_0/\rho) / [1 - \lambda (1 - \rho_0/\rho)]^2$$
 (5)

where  $\rho_{\theta}(V_{\theta})$  and  $\rho(V)$  are the density (specific volumes) of iron at ambient and shock compression, 436 respectively;  $\gamma$  is the Grüneisen parameter of iron along the Hugoniot state (17, 72);  $C_0$  and  $\lambda$  are the Hugoniot parameters, where  $U_s$  (km/s) = 3.935 + 1.578 with  $\rho_0$  = 7.850(2) g cm<sup>-3</sup> for iron (73). The  $V_p$  of 438 hcp-Fe is significantly reduced by elevated temperature, especially above  $T/T_m > \sim 0.74$  ( $P_H \sim 160$  GPa). We used a third-order polynomial to fit the measured  $V_p$  with pressure as  $V_p$  (km/s) = 6.9 + 0.011  $P_H$  + 1.15E-4  $P_H^2$  - 4.61E-7  $P_H^3$  in the investigated pressure range. The fitted curve gives a maximum  $V_p$  of  $\sim$ 10.02 km/s at  $\sim$ 206 GPa. 442

The Poisson's ratio of iron can be determined from the measured  $V_p$ ,  $V_b$ , and  $V_s$  in the present work using the following equation:

445 
$$v = \frac{1}{2} \left[ 1 - \frac{1}{\left( V_p / V_s \right)^2 - 1} \right] = 1 - \frac{2}{3 \left( V_b / V_p \right)^2 + 1}$$
 (6)

The uncertainty of the measured sound velocities under shock compression were estimated through the uncertainty propagation using:

$$\sigma_{V_p} = \sqrt{\left(\frac{\partial V_p}{\partial \delta} \sigma_{\delta}\right)^2 + \left(\frac{\partial V_p}{\partial \Delta t} \sigma_{\Delta t}\right)^2 + \left(\frac{\partial V_p}{\partial U_s} \sigma_{U_s}\right)^2 + \left(\frac{\partial V_p}{\partial \rho_H} \sigma_{\rho_H}\right)^2}$$
(7)

$$\sigma_{V_s} = \sqrt{\left(\frac{\partial V_s}{\partial V_p} \sigma_{V_p}\right)^2 + \left(\frac{\partial V_s}{\partial V_b} \sigma_{V_b}\right)^2} \tag{8}$$

The uncertainties in the sample thickness ( $\delta$ ) and the travel time of shock wave in the sample ( $\Delta t$ ) were measured to be  $\sim 0.1\%$  and  $\sim 1\%$ , respectively. As shown in SI Appendix Fig. S3, the measured  $\Delta t$  has a generally small error of 1-2 ns, with a total time interval of 120-330 ns. Based on the equations (2) and (7), the uncertainties of  $V_p$  and  $V_b$  are estimated to be ~2%. The uncertainty of  $V_s$  is estimated to be between 5% and 15% by using the equations (3) and (8).

**DFT calculations at finite temperature and AIMDs.** In this study, DFT calculations, including structure optimizations and AIMD simulations, are carried out by using the Vienna ab initio simulation (VASP) code (74). The projector augmented-wave (PAW) potentials (75) and the Perdew-Burke-Ernzerhof (PBE) Exchange-correlation functional (76) were employed in the calculations. Considering extreme P-T conditions, a 750-eV energy cutoff potential with 16 valence electrons was used, which sufficiently avoided any overlapping of core states. To ensure accuracy, all necessary tests were conducted and the electronic energy was converged within 1 meV per atom. The optimization of hcp-Fe at 0 K was achieved using a primitive cell with a grid density of 0.025×2Π Å<sup>-1</sup> for *k* point sampling in the Brillouin zone at 230 GPa. A series of *ab initio* NPT (constant number of atoms, pressure, and temperature) molecular dynamics (77) with Langevin thermostat (78) were performed with a time step of 1 fs to access the proper c/a ratio of hcp-Fe at 230 GPa and finite temperature up to melting (3000-10000 K). The NPT AIMD simulation cells consisted of a 4×4×3 supercell for the 4-atom C-centered cell in hcp structure with orthogonal axes and used Γ-point sampling. These data were utilized to train the initial machine learning model during the Concurrent machine learning.

Concurrent machine learning. In this work, we utilized an end-to-end deep learning model called Deep MD (79, 80) to build a potential energy surface (PES) using a dataset generated by DFT calculations. This model has been applied to various systems and has demonstrated credible results, including high-pressure calcium (28) and water (81). In addition, it is important to note that a high-quality dataset is crucial for effectively training the model and achieving a more accurate representation of the phase space. Recently, a novel learning procedure with on-the-fly properties was proposed (82), which has been dubbed concurrent learning as the data is generated in real-time as the training progresses.

We have leveraged our workflow and DFT results to construct a deep learning potential. The construction process involves three parts, as illustrated in *SI Appendix* Fig. S5. Initially, we employed data comprising energy, atomic force, and stress from AIMD simulations of perfect hcp-Fe and hcp-Fe with vacancies to train three initial models with different initialized parameters. Subsequently, we utilized these models to explore a much broader phase space, thereby expediting the process. We then applied an error indicator to identify configurations that were inadequately predicted by the initial models. Those configurations were subjected to DFT self-consistent calculations, and the results were integrated into the dataset. With the aid of this improved dataset, we developed new models with enhanced predictive capabilities that could better anticipate the phase space. This procedure was iterated several times (in our study, three times) until we had acquired a reliable potential with DFT accuracy, as demonstrated in *SI Appendix* Fig. S6. Additionally, in step 2, we investigated various hcp-Fe structures, including perfect crystal, vacancies, twin crystals, grain boundaries, and a mixture of solid and liquid as depicted in *SI Appendix* Fig. S7. This rigorous examination guarantees that our models are practical for a variety of applications.

Machine learning molecular dynamics. Machine Learning Molecular Dynamics (MLMD) were carried out using the LAMMPS code, employing periodic boundary conditions and a time step of 1 fs (83). The simulations comprised a range of particle number from 6912 to 80640 and were conducted for up to nsscale durations. We tested the fluctuations in temperature and diagonal stress tensors of iron at 230 GPa and various temperatures using machine learning simulations with different supercell cell sizes ranging from 144 atoms (a typical size in ab initio simulations) to 31104 atoms (see *SI Appendix* Fig. S14).

Melting point calculation by the two-phase method using machine learning. Theoretical determination of the melting point typically involves comparing free energies of solid and liquid phases or employing direct molecular dynamics (MD). One method for determining the melting point of a substance involves directly heating it from the low-temperature phase until it transforms into a liquid. The temperature at which this transition occurs is typically considered to be the melting point. However, this method tends to overestimate the melting temperature due to the superheating effect. Using this one-phase method, the melting point of iron at 230 GPa was calculated to be ~6600K, which is much higher than the experimental value. Various factors may contribute to this superheating issue, such as the simulation cells with only a small number of atoms compared to real systems, particularly in DFT calculations. Consequently, in finite-time simulations, this method often lacks the full distribution of phase space, causing the melting of the

system to lag behind the temperature rise. Additionally, heating from a perfect solid to melting is an idealized process, with a transition barrier much higher than in real systems with interfaces.

506

507

508

509

510

511

512

513

514

515

516

517

518

519520

521

522

523

524

525

526

527

528

529

534

535

536

537

538539

540

541542

543544

545

546

To address this issue, an improved MD method was proposed, called the two-phase method or coexistence melting method. This method involves simulating a mixture of solid and liquid at different temperatures, allowing solid and liquid to compete with each other. The addition of liquid broadens the phase-space distribution of the system. As melting occurs, their free energy becomes equal, allowing the solid and liquid to coexist. However, this method requires a larger cell to accommodate two states and is not commonly used in AIMDs. With the aid of machine learning potential, it's now feasible to construct a large box and simulate the melting behavior of hcp-Fe in nanosecond scale. Initially, we heated the perfect hcp-Fe with orthogonal axes until it turned into a fully melted liquid. We then integrated it with an initial solid to form a larger supercell, containing up to 80640 atoms. To avoid any unreasonable structures, like the occurrence of atoms that are too close to each other at the solid-liquid interface, we added a vacuum layer with a thickness of 1 Å to the interface (as illustrated in SI Appendix Fig. S7), which could be relaxed during the following NPT simulations. Using this coexistence box, a series of NPT machine learning molecular dynamics simulations were conducted, and the length of the simulations was up to 0.5 ns to ensure proper systems convergence. We then calculated the free energy of the solid and liquid iron at constant pressure and different temperatures. The temperature at which the free energies of solid and liquid iron are equal is known as the temperature of solid-liquid coexistence or the melting point. The melting point of hcp-Fe at 230 GPa was determined to be 5350-5400 K at 230 GPa and 6200-6300 K at 330 GPa (asterisks in SI Appendix Fig. S8), below which the collective atomic motion occurs at  $T/T_m \sim 0.96$ . Our calculated melting point of high-pressure hcp-Fe are in close to the previous work using the similar twophase method(23) and are also consistent with recent high P-T experiments (17-21).

Van Hove self-correlation functions. The van Hove self-correlation function  $P(\Delta r, t)$  gives the probability of an atom at distance  $\Delta r$  after a time interval t. It is defined as,

530 
$$P(\Delta r, t) = \frac{1}{N} \left\langle \sum_{i=1}^{N} \delta(r - |\vec{r}_i(t_0 + t) - \vec{r}_i(t_0)|) \right\rangle_{t_0}$$
(9)

where  $\vec{r}_i(t_0)$  is the position of *i*th atom at a time  $t_0$ , N is the number of atoms, and  $\langle ... \rangle_{t_0}$  is the average of time ensemble. In our simulations, we used 0.1 ns trajectories as the lag time *t* and 0.05 ns trajectories as the time window of ensemble average.

Finite-temperature lattice dynamics. To obtain the 0 K phonon dispersions, lattice dynamics calculations were performed using the phonopy package (84). A  $4\times4\times3$  hcp-Fe supercell, comprising a 2-atom primitive cell and a grid of  $0.025\times2\Pi$  Å<sup>-1</sup> for k points was utilized in the simulation. The renormalized phonon spectra including anharmonicity and temperature-dependent phonon properties were determined at finite temperature using the dynaphopy package (85). The same iron supercell ( $4\times4\times3$ ) was used to perform the MLMDs at varying temperatures with a 1-fs timestep and the 50-ps simulation time. The velocity-autocorrelation functions via MD were analyzed by projecting them onto the harmonic modes, which were calculated in the 0 K phonon calculations. Further theoretical details can be found in Ref. (85). The lattice dynamics calculated using DFT and ML at 0 K are compared in *SI Appendix* Fig. S6e.

Calculation for Poisson's ratio in hcp-Fe near melting. When stretching or compressing a material, it can undergo changes in both axial and transverse directions, which is referred to as the Poisson effect. Poisson's ratio (v) quantifies this phenomenon and is defined as follows:

$$\varepsilon_{axial} = dl_{axial}/l_{axial}$$

547 
$$\varepsilon_{trans} = dl_{trans}/l_{trans}$$

$$v = \frac{-\varepsilon_{trans}}{\varepsilon_{avial}}$$
 (10)

549 where l, dl, and  $\varepsilon$  are length, changes in length and strain along transverse and axial (subscript: trans and 550 axial) directions under certain axial stress.

Non-equilibrium machine learning molecular dynamics (NEMLMD) calculations were conducted to directly simulate the Poisson effect. The NEMLMD simulations were performed using the LAMMPS code, employing periodic boundary conditions and a time step of 1 fs (ref. (83)). In these calculations, tensile stresses were incrementally applied to completely relaxed equilibrium states, derived from two-phase equilibrium molecular dynamics, to achieve a strain  $\varepsilon_{axial}$  of 0.05 (see *SI Appendix* Fig. S10). Throughout the deformation process, the temperature was regulated using a Nose-Hoover thermostat, while the pressure on those two dimensions perpendicular to the deformation direction remained fixed at 230 GPa. These deformations encompassed the Poisson effect, and the change in volume under the deformation is given by:

$$\frac{dV}{V} = \frac{l_{axial} \times l_{trans}^2 \times (1 + \varepsilon_{axial})(1 + \varepsilon_{trans})^2 - l_{axial} \times l_{trans}^2}{l_{axial} \times l_{trans}^2}$$
(11)

Combining the definition in equation (10), for a very small value of strain (here 0.05 scale), the first-order approximation yields:

$$\frac{dV}{V} \approx \varepsilon_{axial} + 2\varepsilon_{trans} = \varepsilon_{axial}(1 - 2v) = dl_{axial}/l_{axial}(1 - 2v)$$
 (12)

When the Poisson's ratio  $\nu$  equals 0.5, the volume remains unchanged by applied stress, rendering the 563 system an incompressible state, such as a liquid. By examining the correlation between  $\frac{dV}{V}$  and  $\frac{dl_{axial}}{l_{axial}}$  at 230 564 GPa and various temperatures (see SI Appendix Fig. S10), we can ascertain the value of  $\nu$  through a linear 565 fitting. Utilizing this approach at room temperature, the Poisson's ratio of hcp-Fe at 230 GPa is 566 approximately 0.36, aligning with some previous experimental findings (10, 11). At temperature  $T/T_m$  of 567 approximately 0.96-0.98, the Poisson's ratio of hcp-Fe at 230 GPa is determined to be approximately 0.44, 568 and the value derived from the calculated elastic constants using the Voigt average scheme (32) at  $T/T_m \sim$ 569 570 0.98 is 0.447.

Movies and Snapshots of deep learning simulations. Movies and snapshots of deep learning simulations are rendered using visual molecular dynamics (VMD) (86) and OVITO (87).

# References

551

552

553554

555

556

557

558

559

562

571572

573574

575576

- 1. A. M. Dziewonski, D. L. Anderson, Preliminary reference Earth model. *Phys. Earth Planet. Inter.* **25**, 297-356 (1981).
- 578 2. J. Li, Y. Fei, "Experimental Constraints on Core Composition" in Treat. Geochem., K. K. Turekian, Ed. (Elsevier, Oxford, 2014), pp. 527-557.
- 580 3. Y. Zhang, J. F. Lin, Molten iron in Earth-like exoplanet cores. *Science* 375, 146-147 (2022).
- J. Aubert, C. C. Finlay, A. Fournier, Bottom-up control of geomagnetic secular variation by the Earth's inner core. *Nature* **502** (2013).
- 583 5. M. Landeau, J. Aubert, P. Olson, The signature of inner-core nucleation on the geodynamo. *Earth. Planet. Sci. Lett.* **465**, 193-204 (2017).
- 585 6. H. Tkalčić, T.-S. Pham, Shear properties of Earth's inner core constrained by a detection of *J* waves in global correlation wavefield. *Science* **362**, 329-332 (2018).
- 587 7. L. Vočadlo, Ab initio calculations of the elasticity of iron and iron alloys at inner core conditions: Evidence for a partially molten inner core? *Earth Planet. Sci. Lett.* **254**, 227-232 (2007).

- 589 8. Y. Li, L. Vočadlo, J. P. Brodholt, The elastic properties of hcp-Fe alloys under the conditions of the Earth's inner core. *Earth Planet. Sci. Lett.* **493**, 118-127 (2018).
- 591 9. G. N. Greaves, A. L. Greer, R. S. Lakes, T. Rouxel, Poisson's ratio and modern materials. *Nat. Mater.* **10**, 823-837 (2011).
- 593 10. H. K. Mao et al., Phonon density of states of iron up to 153 gigapascals. Science 292, 914-916 (2001).
- 594 11. C. A. Murphy, J. M. Jackson, W. Sturhahn, Experimental constraints on the thermodynamics and sound velocities of hcp-Fe to core pressures. *J. Geophys. Res.: Solid Earth* **118**, 1999-2016 (2013).
- 596 12. J. C. E. Irving, Earth's soft heart. *Science* **362**, 294-294 (2018).
- 597 13. F. Nimmo, "Energetics of the Core" in Treat. Geophys., G. Schubert, Ed. (Elsevier, Oxford, 2015), vol. 8, pp. 27-55.
- 599 14. A. Deuss, Heterogeneity and anisotropy of Earth's inner core. *Annu. Rev. Earth Planet. Sci.* **42**, 103-126 (2014).
- T. Wang, X. Song, H. H. Xia, Equatorial anisotropy in the inner part of Earth's inner core from autocorrelation of earthquake coda. *Nat. Geosci.* **8**, 224-227 (2015).
- 603 16. S. Labrosse, J.-P. Poirier, J.-L. Le Mouël, On cooling of the Earth's core. *Phys. Earth Planet. Inter.* **99**, 1-17 (1997).
- J. Li *et al.*, Shock melting curve of iron: a consensus on the temperature at the Earth's inner core boundary. *Geophys. Res. Lett.*, Submitted (2020).
- 5. Anzellini, A. Dewaele, M. Mezouar, P. Loubeyre, G. Morard, Melting of iron at Earth's inner core boundary based on fast X-ray diffraction. *Science* **340**, 464-466 (2013).
- 609 19. S. J. Turneaure, S. M. Sharma, Y. M. Gupta, Crystal structure and melting of Fe shock compressed to 273 GPa: in situ x-ray diffraction. *Phys. Rev. Lett.* **125**, 215702 (2020).
- 611 20. R. G. Kraus *et al.*, Measuring the melting curve of iron at super-Earth core conditions. *Science* **375**, 202-205 (2022).
- G. Morard *et al.*, Solving Controversies on the Iron Phase Diagram Under High Pressure. *Geophys. Res. Lett.* **45**, 11,074-011,082 (2018).
- T. Sun, J. P. Brodholt, Y. Li, L. Vočadlo, Melting properties from ab initio free energy calculations: Iron at the Earth's inner-core boundary. *Phys. Rev. B* **98**, 224301 (2018).
- D. Alfè, G. Price, M. Gillan, Iron under Earth's core conditions: liquid-state thermodynamics and highpressure melting curve from ab initio calculations. *Phys. Rev. B* **65**, 165118 (2002).
- 619 24. K. Hirose, B. Wood, L. Vočadlo, Light elements in the Earth's core. *Nat. Rev. Earth Environ.* **2**, 645-658 (2021).
- J. G. Dash, A. W. Rempel, J. S. Wettlaufer, The physics of premelted ice and its geophysical consequences.
   *Rev. Mod. Phys.* 78, 695-741 (2006).
- A. Samanta, M. E. Tuckerman, T.-Q. Yu, W. E, Microscopic mechanisms of equilibrium melting of a solid. *Science* **346**, 729-732 (2014).
- 625 27. C. J. Wu, P. Söderlind, J. N. Glosli, J. E. Klepeis, Shear-induced anisotropic plastic flow from body-centredcubic tantalum before melting. *Nat. Mater.* **8**, 223 (2009).
- 427 28. Y. Wang *et al.*, Electronically driven 1D cooperative diffusion in a simple cubic crystal. *Phys. Rev. X* 11, 011006 (2021).
- 629 29. J.-F. Lin et al., Sound Velocities of Hot Dense Iron: Birch's Law Revisited. Science 308, 1892-1894 (2005).
- 630 30. B. Martorell, L. Vočadlo, J. Brodholt, I. G. Wood, Strong Premelting Effect in the Elastic Properties of hcp-631 Fe Under Inner-Core Conditions. *Science* **342**, 466-468 (2013).
- 632 31. C. Prescher *et al.*, High Poisson's ratio of Earth's inner core explained by carbon alloying. *Nat. Geo.* **8**, 220-223 (2015).
- 434 32. Y. He *et al.*, Superionic iron alloys and their seismic velocities in Earth's inner core. *Nature* **602**, 258-262 (2022).
- 33. X. Sha, R. E. Cohen, First-principles thermal equation of state and thermoelasticity of hcp Fe at high pressures. *Phys. Rev. B* **81**, 094105 (2010).
- 34. X. Sha, R. E. Cohen, Elastic isotropy of ε-Fe under Earth's core conditions. *Geophys. Res. Lett.* 37, L10302 (2010).
- S. Merkel, H. P. Liermann, L. Miyagi, H. R. Wenk, In situ radial X-ray diffraction study of texture and stress during phase transformations in bcc-, fcc- and hcp-iron up to 36 GPa and 1000 K. *Acta Mater.* **61**, 5144-5151 (2013).
- A. E. Gleason, W. L. Mao, Strength of iron at core pressures and evidence for a weak Earth's inner core. *Nat. Geosci.* **6**, 571 (2013).
- 645 37. H.-R. Wenk, S. Matthies, R. Hemley, H.-K. Mao, J. Shu, The plastic deformation of iron at pressures of the

- Earth's inner core. *Nature* **405**, 1044 (2000).
- S. Merkel, M. Gruson, Y. Wang, N. Nishiyama, C. N. Tomé, Texture and elastic strains in hcp-iron plastically deformed up to 17.5 GPa and 600 K: experiment and model. *Model. Simul. Mater. Sci. Eng.* **20**, 024005 (2012).
- 650 39. M. C. Brennan *et al.*, High-Pressure Deformation of Iron–Nickel–Silicon Alloys and Implications for Earth's Inner Core. *J. Geophys. Res.: Solid Earth* **126**, e2020JB021077 (2021).
- W. Wang *et al.*, Strong shear softening induced by superionic hydrogen in Earth's inner core. *Earth Planet. Sci. Lett.* **568**, 117014 (2021).
- A. B. Belonoshko *et al.*, Stabilization of body-centred cubic iron under inner-core conditions. *Nat. Geosci.* **10**, 312 (2017).
- 42. Z. Wu, W. Wang, Shear softening of earth's inner core as indicated by its high poisson ratio and elastic anisotropy. *Fundam. Res.* https://doi.org/10.1016/j.fmre.2022.08.010 (2022).
- 658 43. M. Ghosh, S. Zhang, L. Hu, S. Hu, Cooperative diffusion in body-centered cubic iron in Earth and super-Earths' inner core conditions. *J. Phys. Condens. Matter* **35**, 154002 (2023).
- 660 44. S. Tateno, K. Hirose, Y. Ohishi, Y. Tatsumi, The structure of iron in Earth's inner core. *Science* **330**, 359-361 (2010).
- 662 45. S. Singh, M. Taylor, J. Montagner, On the presence of liquid in Earth's inner core. *Science* **287**, 2471-2474 (2000).
- 46. Y. Zhang, P. Nelson, N. Dygert, J.-F. Lin, Fe alloy slurry and a compacting cumulate pile across Earth's inner-core boundary. *J. Geophys. Res.: Solid Earth* **124**, 10954-10967 (2019).
- J. M. Brown, R. G. McQueen, Phase transitions, Grüneisen parameter, and elasticity for shocked iron between 77 GPa and 400 GPa. *J. Geophys. Res.* **91**, 7485-7494 (1986).
- 48. J. H. Nguyen, N. C. Holmes, Melting of iron at the physical conditions of the Earth's core. *Nature* **427**, 339-342 (2004).
- T. Sakamaki *et al.*, Constraints on Earth's inner core composition inferred from measurements of the sound velocity of hcp-iron in extreme conditions. *Science advances* **2**, e1500802 (2016).
- 50. D. Antonangeli *et al.*, Sound velocities and density measurements of solid hcp-Fe and hcp-Fe–Si (9 wt.%) alloy at high pressure: Constraints on the Si abundance in the Earth's inner core. *Earth Planet. Sci. Lett.* **482**, 446-453 (2018).
- 51. D. Ikuta *et al.*, Sound velocity of hexagonal close-packed iron to the Earth's inner core pressure. *Nat. Commun.* **13**, 7211 (2022).
- 677 52. C. S. Yoo, N. C. Holmes, M. Ross, D. J. Webb, C. Pike, Shock temperatures and melting of iron at Earth core conditions. *Phys. Rev. Lett.* **70**, 3931-3934 (1993).
- 679 53. H. Huang *et al.*, Inner core composition paradox revealed by sound velocities of Fe and Fe-Si alloy. *Nat. Commun.* **13**, 616 (2022).
- 681 54. Z. Mao *et al.*, Sound velocities of Fe and Fe-Si alloy in the Earth's core. *Proc. Natl. Acad. Sci. USA* **109**, 10239-10244 (2012).
- 55. X. Fan, D. Pan, M. Li, Melting of bcc crystal Ta without the Lindemann criterion. *J. Phys. Condens. Matter* **31**, 095402 (2019).
- 685 56. L. E. Dresselhaus-Marais *et al.*, In situ visualization of long-range defect interactions at the edge of melting. *Sci. Adv.* 7, eabe8311 (2021).
- 57. L. Van Hove, Correlations in space and time and Born approximation scattering in systems of interacting particles. *Phys. Rev.* **95**, 249 (1954).
- 689 58. W. Sturhahn *et al.*, Phonon density of states measured by inelastic nuclear resonant scattering. *Phys. Rev. Lett.* **74**, 3832 (1995).
- 59. Y. Zhang *et al.*, Transport properties of Fe-Ni-Si alloys at Earth's core conditions: Insight into the viability of thermal and compositional convection. *Earth Planet. Sci. Lett.* **553**, 116614 (2021).
- 693 60. T. Komabayashi, Thermodynamics of the system Fe–Si–O under high pressure and temperature and its implications for Earth's core. *Phys. Chem. Miner.* **47**, 32 (2020).
- 695 61. T. Sakairi *et al.*, Sound velocity measurements of hcp Fe-Si alloy at high pressure and high temperature by inelastic X-ray scattering. *Amer. Mineral.* **103**, 85-90 (2018).
- 697 62. S. Dominijanni *et al.*, Sound Velocity Measurements of B2-Fe-Ni-Si Alloy Under High Pressure by Inelastic X-Ray Scattering: Implications for the Composition of Earth's Core. *Geophys. Res. Lett.* **49**, e2021GL096405 (2022).
- 700 63. T. Sakai, E. Ohtani, N. Hirao, Y. Ohishi, Stability field of the hcp-structure for Fe, Fe-Ni, and Fe-Ni-Si alloys up to 3 Mbar. *Geophys. Res. Lett.* **38**, L09302 (2011).
- 702 64. T. Komabayashi et al., Phase relations in the system Fe-Ni-Si to 200 GPa and 3900 K and implications for

703 Earth's core. *Earth Planet. Sci. Lett.* **512**, 83-88 (2019).

747748

- 704 65. J. K. Wicks *et al.*, Crystal structure and equation of state of Fe-Si alloys at super-Earth core conditions. *Science advances* **4**, eaao5864 (2018).
- 706 66. B. A. Buffett, Geodynamic estimates of the viscosity of the Earth's inner core. *Nature* **388**, 571-573 (1997).
- 707 K. Cao *et al.*, Refractive index and phase transformation of sapphire under shock pressures up to 210 GPa. *J. Appl. Phys.* **121**, 115903 (2017).
- 709 68. P. Renganathan, T. S. Duffy, Y. M. Gupta, Sound velocities in shock-compressed soda lime glass: Melting and liquid-state response. *Phys. Rev. B* **104**, 014113 (2021).
- 711 69. T. S. Duffy, T. J. Ahrens, Compressional sound velocity, equation of state, and constitutive response of shock-compressed magnesium oxide. *J. Geophys. Res.: Solid Earth* **100**, 529-542 (1995).
- 713 70. M. Beason, B. Jensen, S. Crockett, Shock melting and the hcp-bcc phase boundary of Mg under dynamic loading. *Phys. Rev. B* **104**, 144106 (2021).
- 71. H. Huang *et al.*, Evidence for an oxygen-depleted liquid outer core of the Earth. *Nature* **479**, 513-516 (2011).
- 716 72. H.-J. Huang, F.-Q. Jing, L.-C. Cai, Y. Bi, Grüneisen Parameter along Hugoniot and Melting Temperature of ε-Iron: a Result from Thermodynamic Calculations. *Chin. Phys. Lett.* **22**, 836-838 (2005).
- 718 73. J. M. Brown, J. N. Fritz, R. S. Hixson, Hugoniot data for iron. J. Appl. Phys. 88, 5496-5498 (2000).
- 719 74. G. Kresse, J. Furthmüller, Efficient iterative schemes for ab initio total-energy calculations using a plane-720 wave basis set. *Phys. Rev. B* **54**, 11169-11186 (1996).
- 721 75. P. E. Blöchl, Projector augmented-wave method. *Phys. Rev. B* **50**, 17953 (1994).
- 722 76. J. P. Perdew, K. Burke, M. Ernzerhof, Generalized Gradient Approximation Made Simple. *Phys. Rev. Lett.* 77, 3865-3868 (1996).
- 724 77. M. Parrinello, A. Rahman, Crystal structure and pair potentials: A molecular-dynamics study. *Phys. Rev. Lett.* 45, 1196 (1980).
- 726 78. G. S. Grest, K. Kremer, Molecular dynamics simulation for polymers in the presence of a heat bath. *Phys.* 727 *Rev. A* **33**, 3628 (1986).
- 728 79. L. Zhang, J. Han, H. Wang, R. Car, E. Weinan, Deep potential molecular dynamics: a scalable model with the accuracy of quantum mechanics. *Phys. Rev. Lett.* **120**, 143001 (2018).
- H. Wang, L. Zhang, J. Han, E. Weinan, DeePMD-kit: A deep learning package for many-body potential energy representation and molecular dynamics. *Comput. Phys. Commun.* **228**, 178-184 (2018).
- 732 81. L. Zhang, H. Wang, R. Car, E. Weinan, Phase Diagram of a Deep Potential Water Model. *Phys. Rev. Lett.* 126, 236001 (2021).
- 734 82. Y. Zhang *et al.*, DP-GEN: A concurrent learning platform for the generation of reliable deep learning based potential energy models. *Comput. Phys. Commun.* **253**, 107206 (2020).
- 736 83. S. Plimpton, Fast parallel algorithms for short-range molecular dynamics. J. Comput. Phys. 117, 1-19 (1995).
- 737 84. A. Togo, I. Tanaka, First principles phonon calculations in materials science. Scr. Mater. 108, 1-5 (2015).
- 738 85. A. Carreras, A. Togo, I. Tanaka, DynaPhoPy: A code for extracting phonon quasiparticles from molecular dynamics simulations. *Comput. Phys. Commun.* **221**, 221-234 (2017).
- 740 86. W. Humphrey, A. Dalke, K. Schulten, VMD: visual molecular dynamics. J. Mol. Graph. 14, 33-38 (1996).
- 741 87. A. Stukowski, Visualization and analysis of atomistic simulation data with OVITO-the Open Visualization
   742 Tool. *Model. Simul. Mater. Sci. Eng.* 18, 015012 (2009).
- 743 88. Y. Zhang *et al.*, Melting curve of vanadium up to 256 GPa: Consistency between experiments and theory. *Phys. Rev. B* **102**, 214104 (2020).
- Q. Liu, X. Zhou, X. Zeng, S. N. Luo, Sound velocity, equation of state, temperature and melting of LiF single crystals under shock compression. *J. Appl. Phys.* 117, 045901 (2015).

Acknowledgments. We acknowledge B. Gan, X.H. Li, Y.X. Hua, and Q.M. Wang for their help in the

shock experiments. We thank S.P. Grand, Y.G. Li, X.L. Sun, R.E. Cohen, P. Driscoll and A.F. Goncharov

for the fruitful discussion. This work was supported by the National Natural Science Foundation of China

- 752 (Grant Nos. 42074098, 12125404, 11974162, and 11834006) and the Fundamental Research Funds for the
- Central Universities (Nanjing University). JFL acknowledges support from the Geophysics Program of the National Science Foundation, USA (EAR-1901801). The calculations were carried out using
- 755 supercomputers at the High-Performance Computing Center of Collaborative Innovation Center of
- Advanced Microstructures, the high-performance supercomputing center of Nanjing University.

- 757 Code availability. Six codes were used to obtain results: VASP for ab initio molecular dynamics (available https://www.vasp.at); LAMMPS for classical molecular dynamics (available 758 http://lammps.sandia.gov); Deep-MD kit and DP-GEN for training machine learning potential (available at 759 760 https://github.com/deepmodeling/deepmd-kit and https://github.com/deepmodeling/dpgen); Phonopy and Dynaphopy for lattice dynamics (available https://phonopy.github.io/phonopy at and 761 762 http://abelcarreras.github.io/DynaPhoPy).
- 763 **Data availability.** All data in the paper are present in the article and/or Supplementary Materials.

# PNAS www.pnas.org

765

777

766 **Supplementary Information for** 767 Collective atomic motion in solid iron at the conditions of Earth's inner core 768 Youjun Zhang, Yong Wang, Yuqian Huang, Junjie Wang, Zhixin Liang, Long Hao, Zhipeng Gao, 769 770 Jun Li, Qiang Wu, Hong Zhang, Yun Liu, Jian Sun, Jung-Fu Lin 771 This PDF file includes: 772 773 Text S1 to S5. Fig. S1 to S14. 774 Table S1. 775 Movie S1. 776

# **Supplementary Text**

Text S1. Solid to liquid phase transition of iron under shock compression. In previous studies, longitudinal sound velocity  $V_p$  of iron under shock compression had been reported to display sharp discontinuities at around 200 GPa and 220 GPa (47, 48). The discontinuity observed at 200 GPa was initially interpreted as indicative of an unknown solid-solid phase transition (47); however, subsequent experiments has refuted this observation (48). In this study, the measured  $V_p$  and  $V_s$  did not show any sharp discontinuity up to the shock pressure of 230 GPa. Instead, our new experiments showed significant sound velocity softening because the shock Hugoniot temperature gradually approaches to the melting point of iron with increasing shock pressure above 200 GPa. This suggests that there was no first-order phase structural transition according to the changes in the measured sound velocity in the pressure range of 200-230 GPa, which further confirmed that only single hcp phase structure without obvious embedded melting was present in solid iron before shock-induced melting using in situ XRD measurements under wellcharacterized shock compression (19, 20). The gradual reduction in sound velocity observed with increasing shock pressure is thought to be caused by the collective atomic motion of premelting hcp-Fe through the atomistic simulations. Notably, when iron was shocked to  $\sim 260$  GPa, the measured  $V_p$  drops down to  $V_b$ , indicating complete melting above this pressure (48). Furthermore, static high P-T experiments also suggest that hcp was the only phase observed in solid iron at conditions relevant to the inner core (44).

Text S2. Dynamical behaviors of iron in hcp solid and liquid state. At 230 GPa and 5000 K (with  $T/T_m \sim 0.92$ ), iron has an ideal hcp structure without any collective motion, as revealed by our ns-scale two-phase simulations (Fig. S11a). Upon further heating to 5500 K using the two-phase method, the system transforms into a liquid state (Fig. S11b). In addition, the van Hove self-correlation functions  $P(\Delta r, t)$  in hcp crystal at 230 GPa and 5000 K displays a stable Gaussian distribution over time, indicating that the atoms vibrate around their equilibrium positions (Fig. S11c). However, in liquid iron at 5500 K,  $P(\Delta r, t)$  diverges over time due to the disorderly diffusion of atoms (Fig. S11d), and its mean square displacements (MSD) of atoms increases rapidly with the whole simulation time (Fig. S12). Furthermore, the collective motion of premelting hcp-Fe at Earth's inner core conditions (approximately 330 GPa and 6000 K with  $T/T_m \sim 0.97$ ) was computed and illustrated in Fig. S13.

Text S3. Two-phase melting model and melting points of hcp-Fe at the core pressure. Collective atomic motion in premelting hcp-Fe can result in significant softening of the shear modulus and an ultrahigh Poisson's ratio. However, the temperature in the shear softening regime calculated using the traditional EMD method is ~1000 K higher than the determined melting point of hcp-Fe in experiments (30). This discrepancy arises from the fact that homogeneous melting in the one-phase model is often accompanied by superheating. The one-phase method does not take into account some subsistent impurities in solid iron such as defects, grain boundaries, and interfaces, which could contribute to initial nucleation on melting.

To accurately reproduce the measured melting points of typical d-block transition metals such as iron, tantalum, and vanadium at high P-T, a two-phase melting model is usually more appropriate (88). For instance, using machine learning simulations with the two-phase model, the melting point of hcp-Fe is estimated to be approximately 5400 K at 230 GPa and 6200-6300 K at 330 GPa, respectively. These values are consistent with experimental determinations of 5300-5500 K and 6000-6300 K obtained by both static (18) and shock (17, 19) experiments (Fig. S8). Consequently, we adopted the two-phase method to investigate the melting behavior and Poisson's ratio of hcp-Fe at the P-T conditions relevant to the inner core.

Text S4. Elastic modulus of hcp-Fe at high pressure-temperature. The elastic modulus of a single crystal hcp-Fe was calculated at different temperatures and a constant pressure of 230 GPa using *ab initio* molecular dynamics (AIMD) method, which was also used in Ref. (30). To create unit cells at different temperatures, the average lattice parameters from NPT (constant number of atoms, pressure, and temperature) AIMDs were employed., NVT (constant number of atoms, volume, and temperature) AIMDs were then carried out on these unit cells and their distortional duplicates of hcp symmetry ( $\pm$  0.02 strain) to compute stresses and corresponding distortions. Through a non-linear  $2^{nd}$  fitting based on these outcomes, the elastic modulus of the system at finite temperatures can be determined. The NVT AIMD simulation cells were constructed of a  $4\times2\times2$  supercell of the 4-atom C-centered cell in hcp structure with orthogonal axes and 4 irreducible k-points.

The calculated elastic modulus of hcp-Fe exhibited a significant reduction before reaching to the melting point  $(T/T_m > \sim 0.95)$  (Fig. 4), consistent with the results predicted in Ref. (30). To confirm the effect of collective motion on the shear modulus, we further employed the machine learning potential to calculate elastic constants of hcp-Fe. Our results indicate that collective atomic motion in premelting hcp-Fe provides a microscopic explanation of the temperature-induced strong shear softening. As a result, both two-phase and one-phase simulations simultaneously revealed the temperature-induced shear softening in premelting hcp-Fe with collective motion in this study.

Text S5. Effect of the supercell size on the calculation. To assess the influence of supercell size on our simulations, we conducted tests to examine the fluctuations in temperature and diagonal stress tensors of iron at 230 GPa and various temperatures using machine learning simulations. We employed cell sizes ranging from 144 atoms (a typical size in ab initio simulations) to 31104 atoms (Fig. S14). The results revealed substantial thermodynamic fluctuations in simulations with smaller cell sizes, such as 144 atoms, leading to relatively large errors in the calculations. However, as the number of atoms increased to approximately 10000, the systems exhibited convergence to the target temperature and pressure, with significantly reduced fluctuations. For instance, the standard deviations in temperature and pressure for simulations with 144 atoms and 18000 atoms were estimated to be 380 K and 31 K, 9.53 GPa and 0.91

GPa, respectively. As a result, the pressure and temperature fluctuations in our simulations were too small to induce iron encompassing between the solid and liquid phases in each run. As our machine learning simulations were based on cells with at least 10000 atoms, we are confident that our data and conclusions are both valid and physically meaningful.

Text S6. Effect of nickel and possible light elements on the collective motion of hcp-Fe in the inner core. Our computations show that the collective atomic motion of hcp-Fe occurs at 330 GPa and a temperature range of 5800-6200 K, which is slightly lower by 0-6% than its melting temperature. However, our study here does not account for the effect of the presence of nickel (Ni) at ~5wt.% and light elements at 2-4 wt.% in the inner core (2). Literature results have demonstrated that adding small quantities of light elements, such as Si and O, to iron can decrease its melting temperature by several hundreds of K at core pressures (60). It is important to note that the collective atomic motion happens in hcp-Fe at a temperature ratio of  $T/T_m > \sim 0.95$ . Given this, the incorporation of light elements (such as Si, S, O, and C) into iron should result in the occurrence of collective motion at a relatively lower temperature due to the reduced melting point. For example, collective motion in hcp-Fe alloys could take place at  $\sim 5200-5500$  K. As a result, it is reasonable to expect that iron alloyed with  $\sim 5$  wt.%Ni and 2-4 wt.% light elements could also display shear wave softening and collective motion nearing melting at relevant P-T conditions of the inner core.

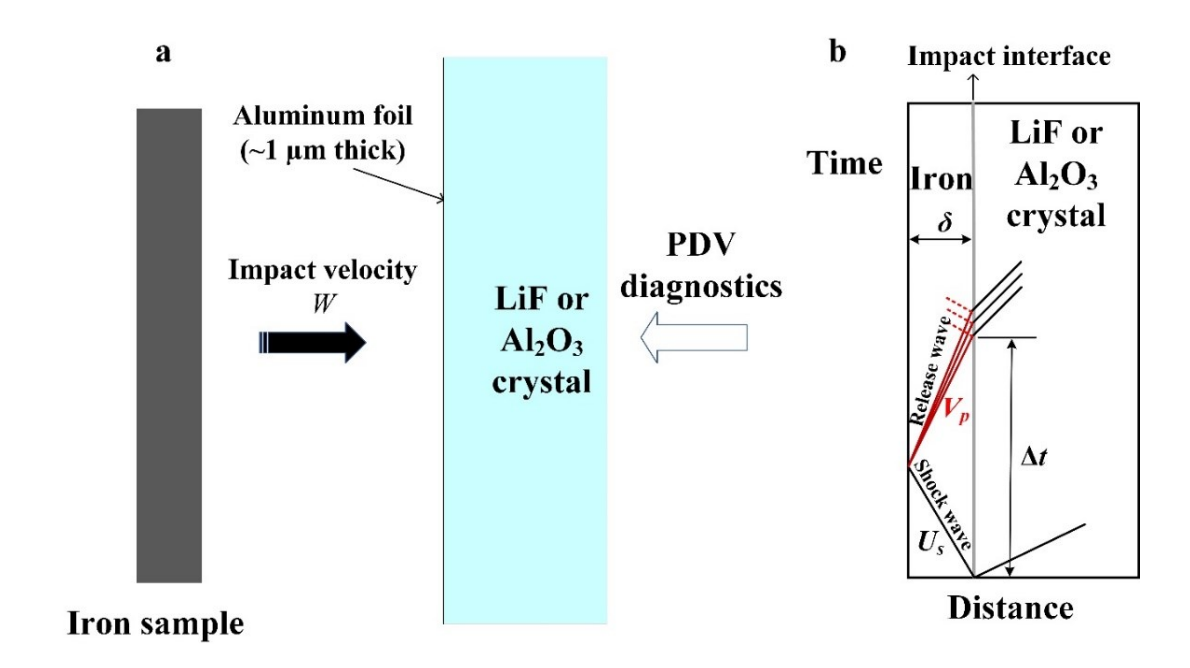


Fig. S1. Schematic diagram of the experimental setup for sound velocity measurements of iron at high pressure-temperature using the reverse-impact method in a two-stage light-gas gun. (a) The reverse-impact method was used to measure both the longitudinal and bulk sound velocities of iron. Photon Doppler velocimetry was used to obtain wave profiles at the iron/window interface. We used <100> LiF or <0001> Al<sub>2</sub>O<sub>3</sub> crystals as transparent windows. W (km/s) represents the impact velocity. A thin aluminum film ( $\sim$ 1  $\mu$ m) was vapor-deposited on the impact surface of the LiF and Al<sub>2</sub>O<sub>3</sub> windows to efficiently reflect the laser light. (b) The relationship between time and Lagrangian distance shows the propagation of shock and release waves in the sample and window after impact.

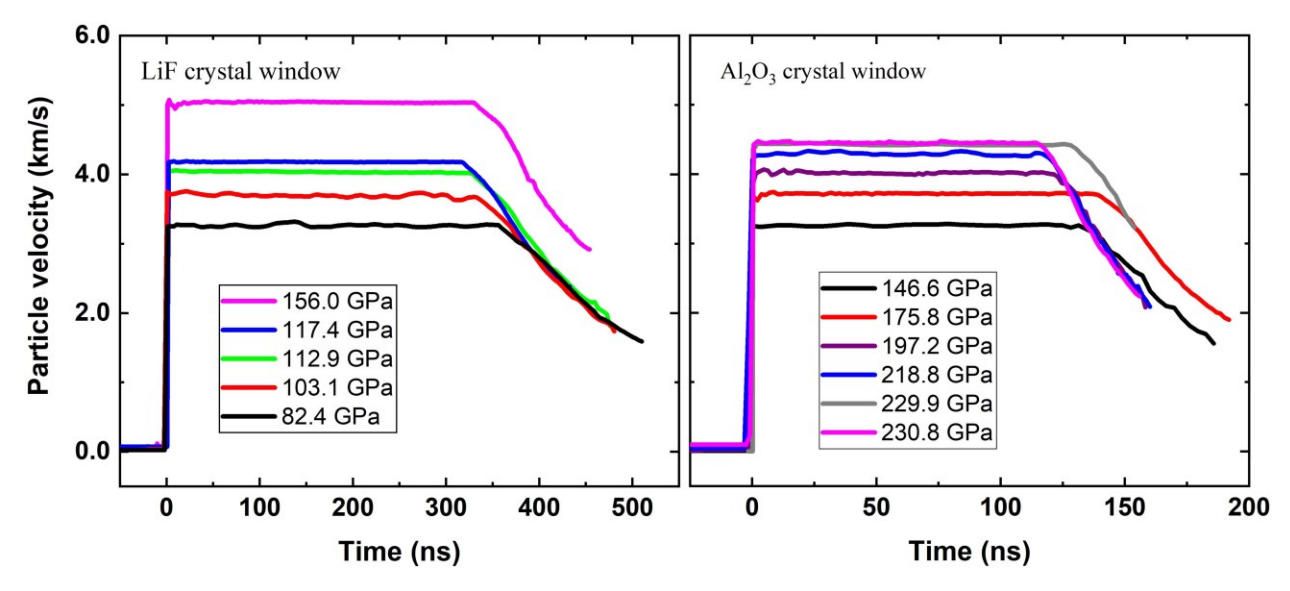


Fig. S2. Particle velocity profiles at the iron/window interface during shock compression. The wave profiles were measured using PDV with a time resolution of  $\sim 1$  ns. The used windows were LiF (left) and Al<sub>2</sub>O<sub>3</sub> crystals (right), respectively. The details of the reverse-impact conditions are listed in Table S1.

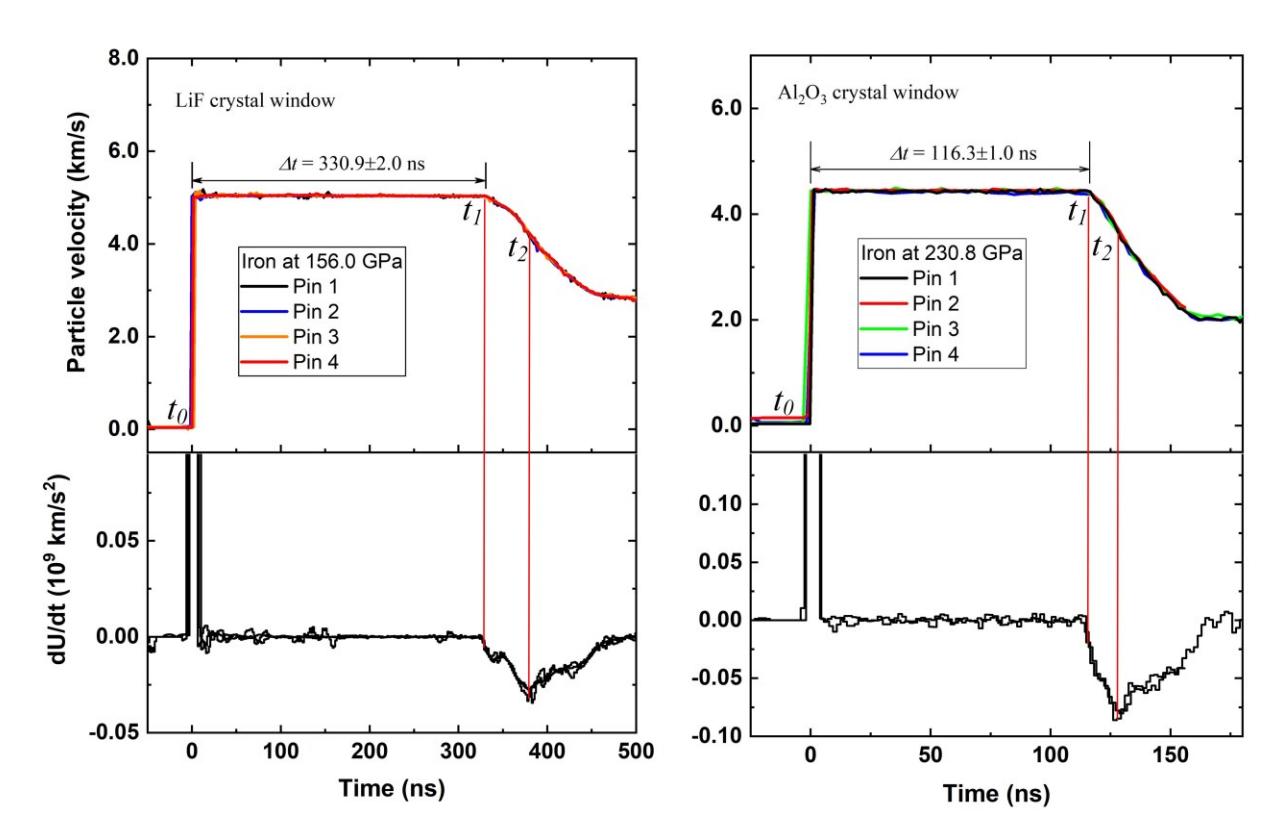


Fig. S3. Typical particle velocity profiles at the interface between iron and windows by multiple pins. The used windows were LiF crystal in shot No. 6 (left) and  $Al_2O_3$  crystal in shot No. 11 (right). The derivative of particle velocity with respect to time, dU/dt, is used to help obtain the time  $t_0$ ,  $t_1$ , and  $t_2$  that correspond to the arrival times of shock wave front, rarefaction wave at the interface, and the elastic-plastic transition point.

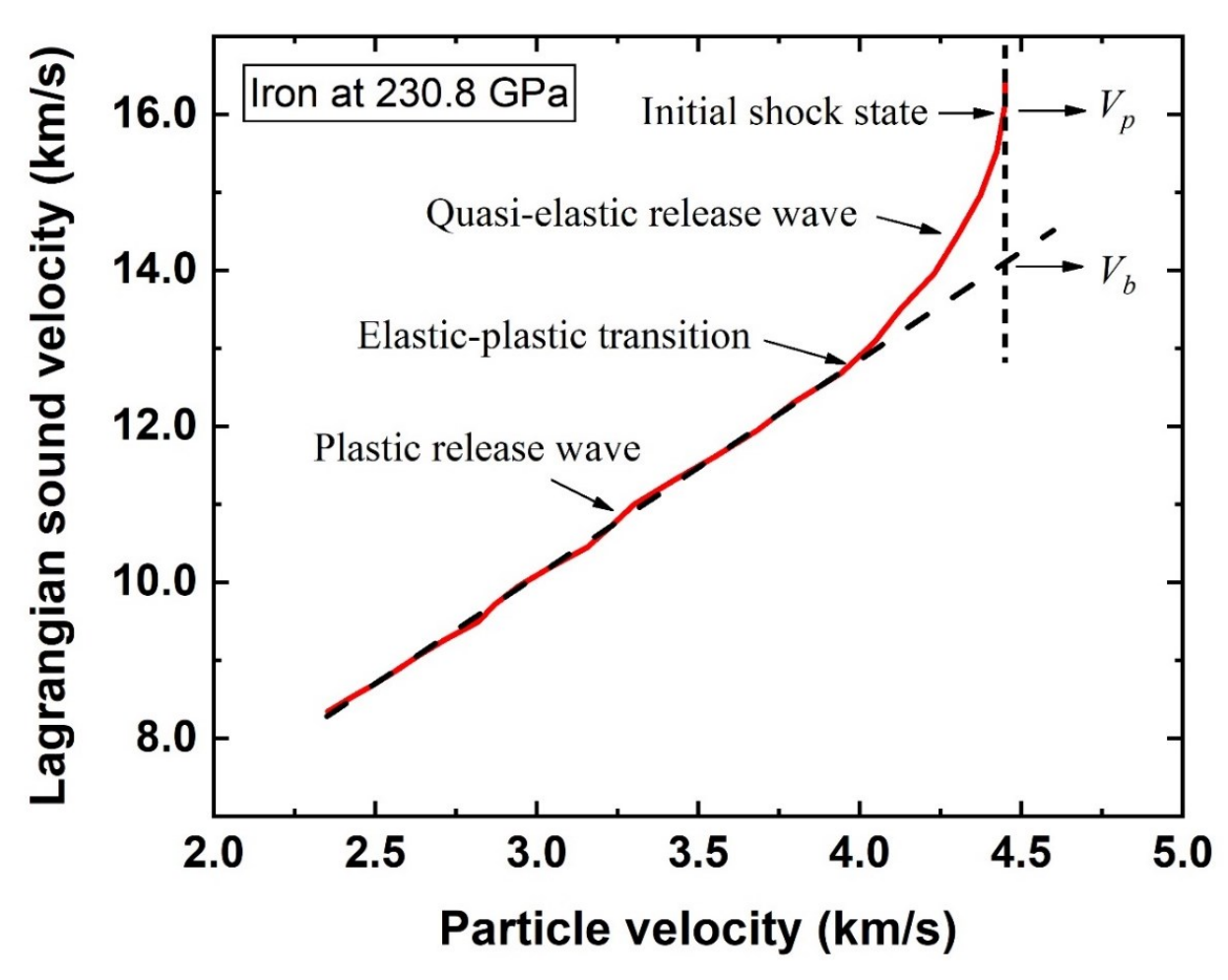


Fig. S4. Typical Lagrangian sound velocity in iron versus the particle velocity. The  $V_b$  of iron can be extrapolated via a linear fitting upon the plastic release wave. The shock pressure is ~230.8 GPa in Shot No. 11.

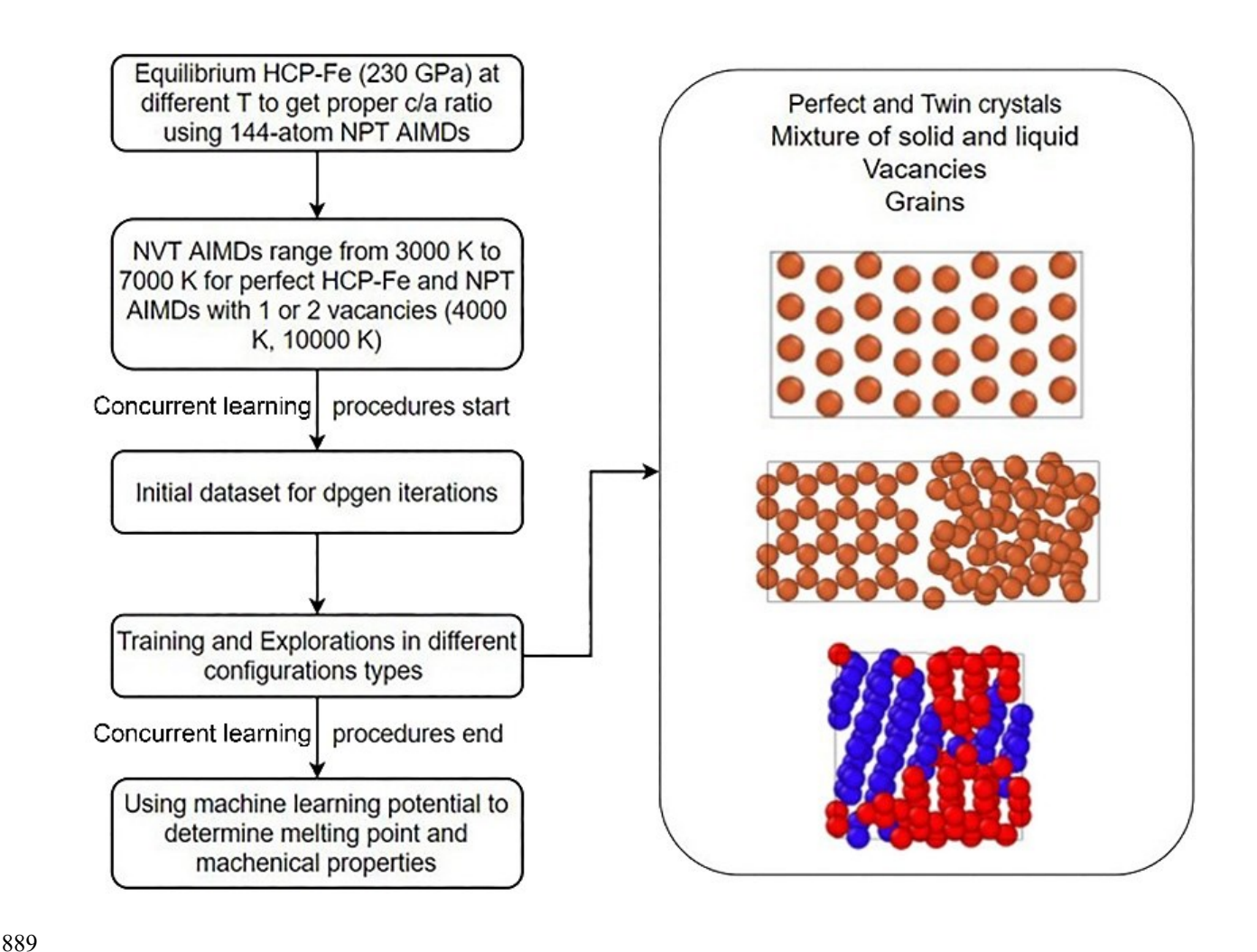
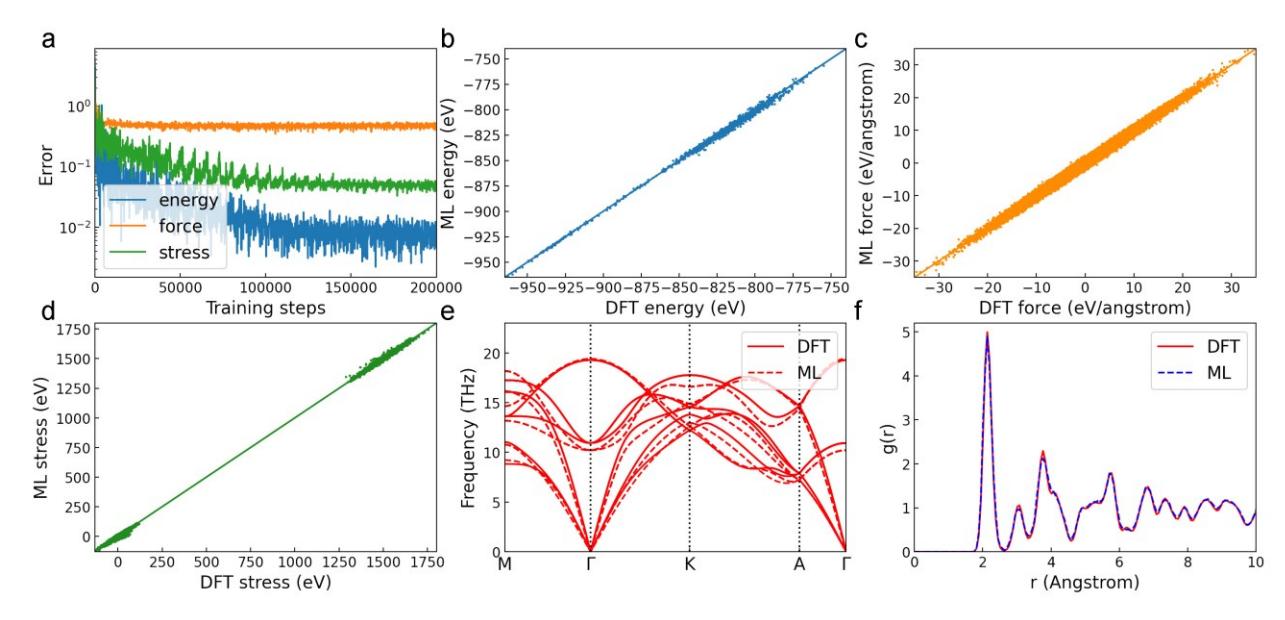


Fig. S5. Schematic illustration of concurrent machine learning procedure in our work. The learning procedure was separated into several parts including initialization, exploration, model deviation, etc. Different configuration types in phase space were considered and learned. More details can be found in Ref. (82).



**Fig. S6. Training errors of the machine learning (ML) and comparisons between DFT results and our machine learning model.** (a) Convergence of training errors (root mean square error) for energy, force, and stress during the machine learning (ML) training. (b-d) Comparisons of energy, force, and stress (shear and normal) between our ML model and DFT calculations. The comparisons show remarkable consistency among these predicted quantities. The solid diagonal lines serve as visual aids to facilitate interpretation. (e-f) Comparisons of lattice dynamics (phonon spectrum) and radial distribution functions g(r) of hcp-Fe at 330 GPa and 0 K between DFT results and our ML model.

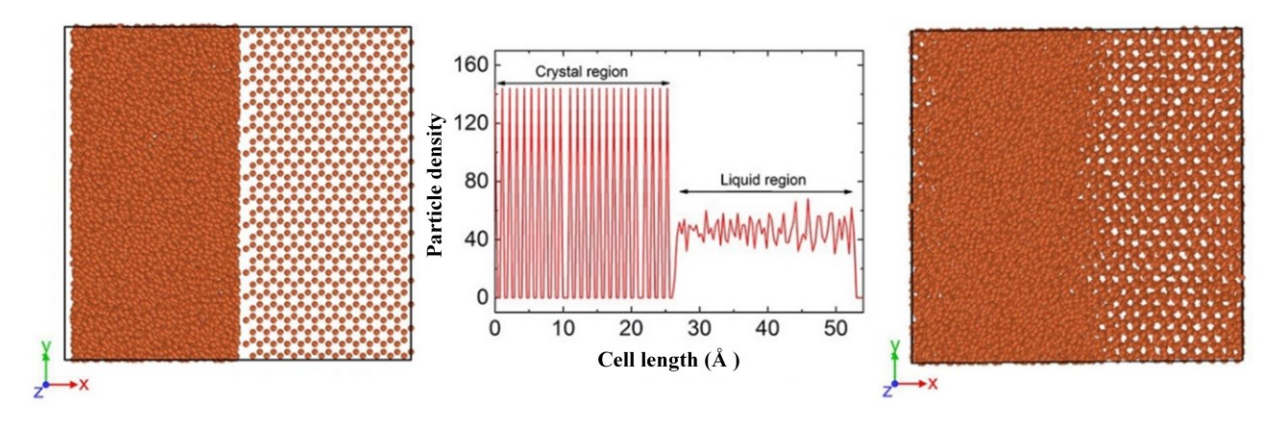


Fig. S7. Initial configuration of iron in two-phase method (left) and its particle density along the x-axis (middle), as well as the final configuration after 50 ps (right). The configuration contains 20160 iron atoms. The NPT simulations were conducted at the melting point of 5350 K at the pressure of 230 GPa and at the melting point of 6200 K at the pressure of 330 GPa, respectively. The initial interface between solid and liquid was divided by a 1 Å vacuum layer to prevent unreasonable structures. The coexistence of solid and liquid in the right figure locates the melting.

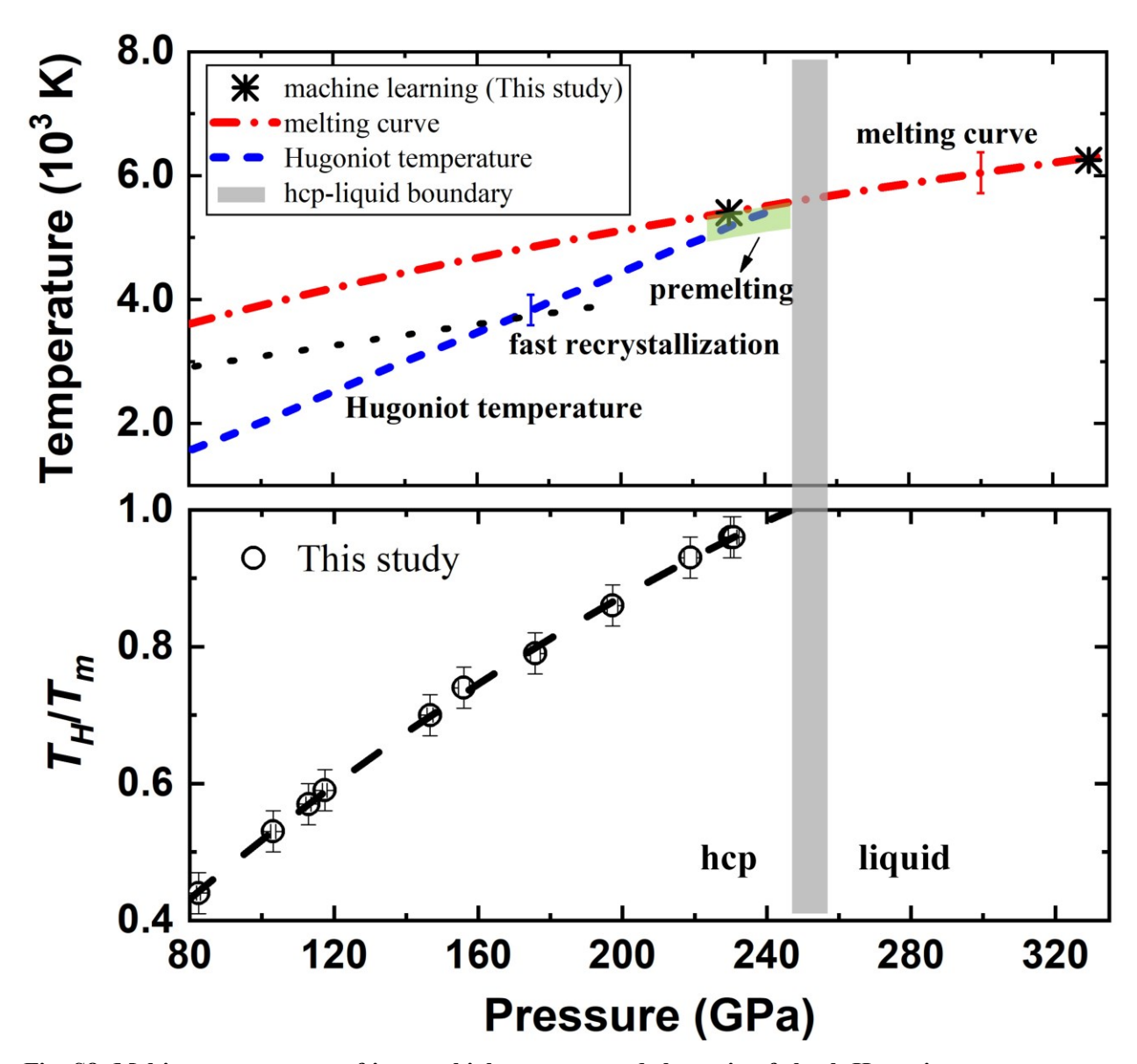


Fig. S8. Melting temperature of iron at high pressure and the ratio of shock Hugoniot temperature to melting point. Top, Pressure vs. temperature relation in shock-compressed iron and the melting curve of iron at high pressure. The \* represents the present calculated melting points of hcp-Fe at 230 GPa and 330 GPa by the two-phase method using machine learning MD. The red dash-dot line represents the melting curve of iron at high pressure from both experiments (17-19) and theoretical computations (22, 23). The blue short-dash line represents the measured Hugoniot temperature in solid iron from literature (17, 19, 23, 52). The light-green region represents the ratio of shock temperature to the melting point of iron above 0.96, where collective atomic motion occurs in iron under shock compression. The temperature threshold for collective motion in solid iron is significantly higher the temperature boundary at which fast recrystallization occurs in polycrystalline iron (black dotted line). Bottom, The ratio of Hugoniot temperature of iron to its melting point ( $T_H/T_m$ ) as a function of shock pressure. Open circles represent the  $T_H/T_m$  conditions in the present sound velocity measurements under shock compression. The hcp-liquid boundary of shocked-iron was determined by *in situ* XRD (19) and sound velocity measurements (48) under shock compression, which happens at 247-260 GPa.

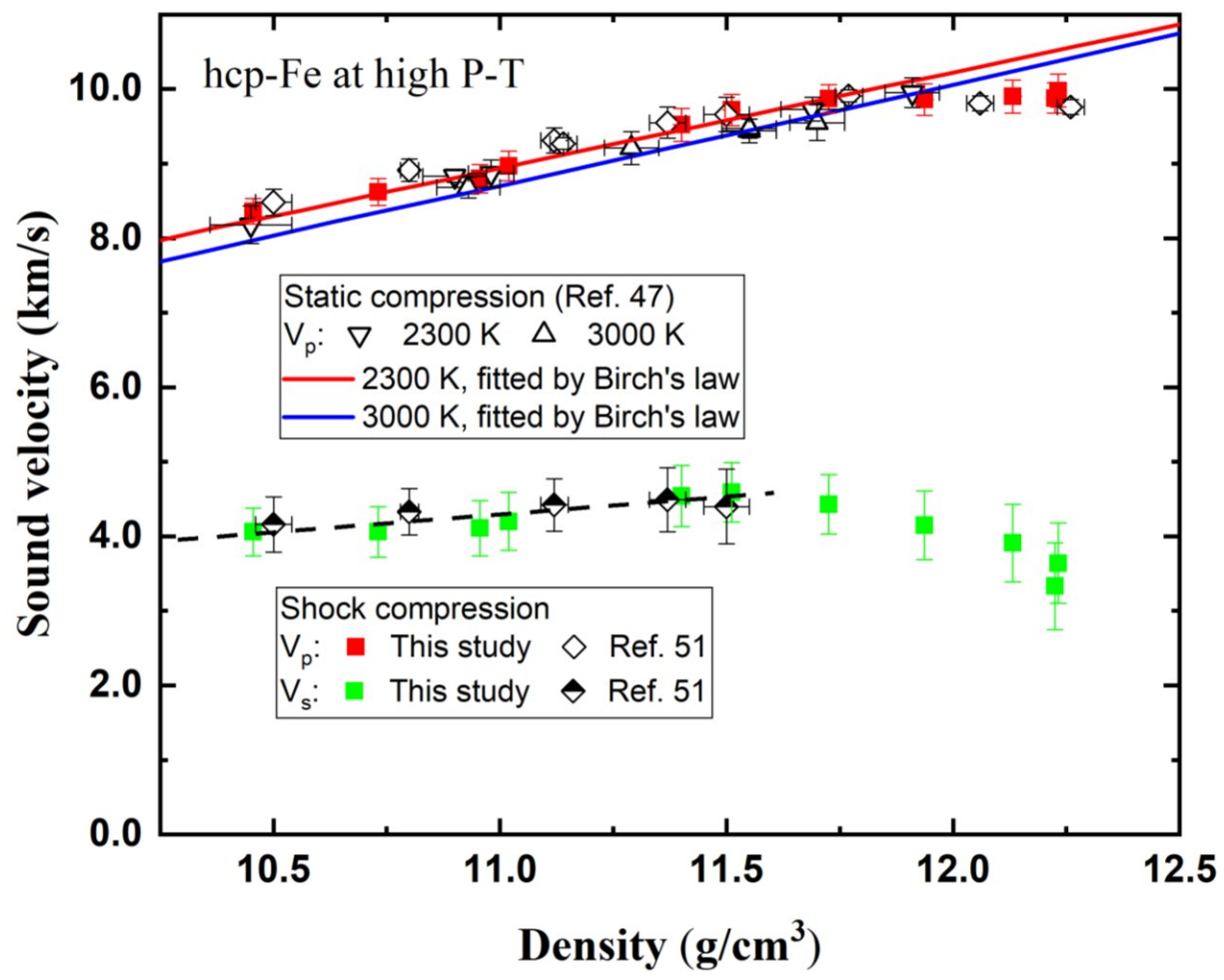
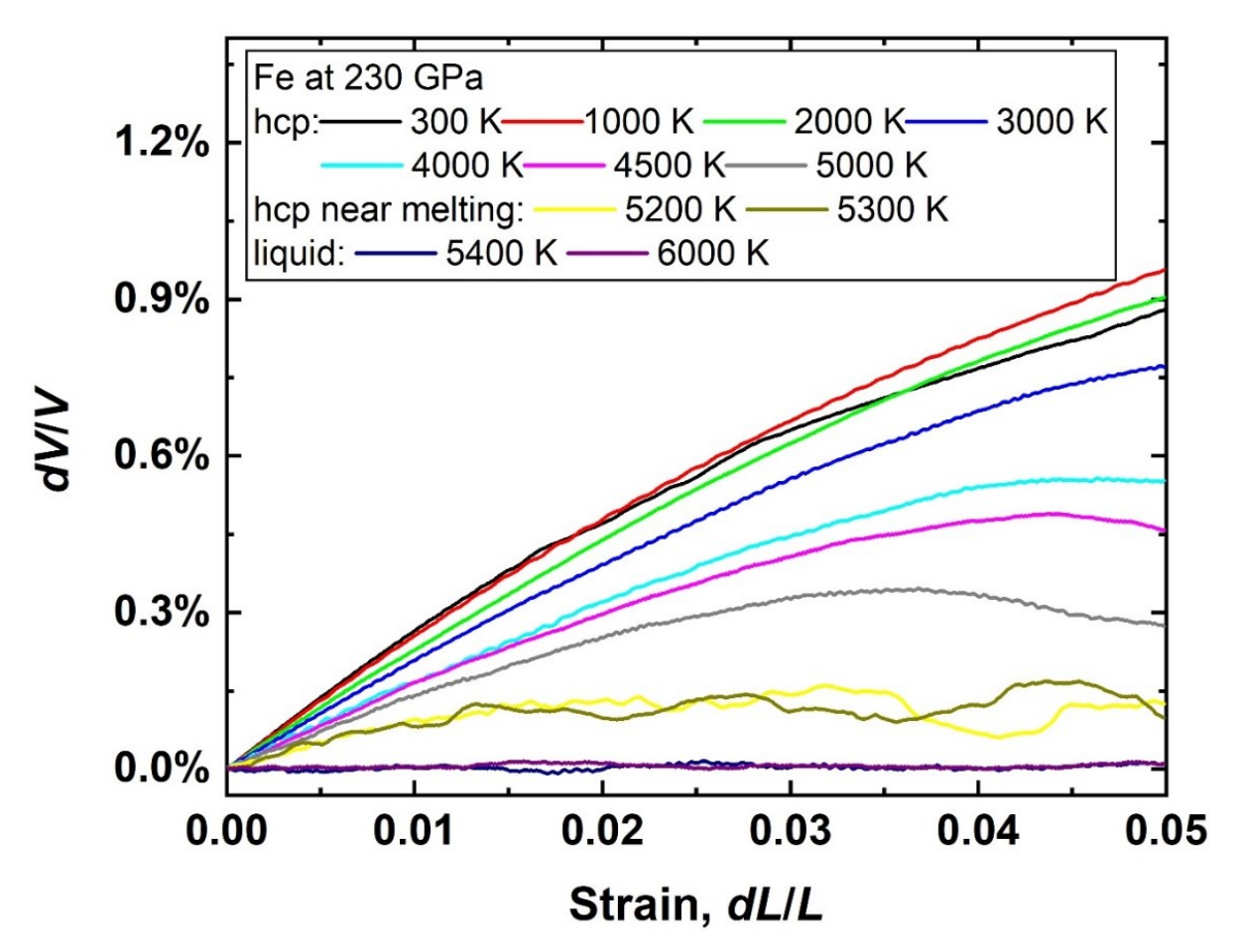


Fig. S9. Sound velocity of hcp-Fe as a function of density under high pressure and temperature conditions by static and shock compression. The  $V_P$  of hcp-Fe up to 163 GPa and 3000 K was measured using inelastic x-ray scattering from a laser-heated sample in a diamond anvil cell (49). The  $V_P$  and  $V_S$  was determined up to 231 GPa and 5200 K under shock compression in this study. At relatively low temperatures (e.g., up to 3000 K), the density-velocity relation of hcp-Fe could be reasonably described by a quasi-linear Birch's law. However, as it approached the premelting region, the sound wave velocity is significantly softened so that the Birch's law is broken down. The quasi-linear dashed-line serves as a visual guide, representing a quasi-linear relationship between the  $V_S$  and density of iron at the relatively low P-T conditions.



**Fig. S10. Volume change vs. gradual deformation under axial strain in hcp-Fe at 230 GPa and different temperatures.** The Poisson's effect could be simulated in this way. The volume change indicates different responses of hcp-Fe. For solid (< 5100 K), the system shows a strong elasticity with a linear increase under a small deformation. For hcp-Fe at near melting point (> 5200 K), collective atomic motion induces the softening and the slope of the volume response curve decreases rapidly. For liquid (> 5400 K), the volume would not change with the deformation due to its incompressibility.

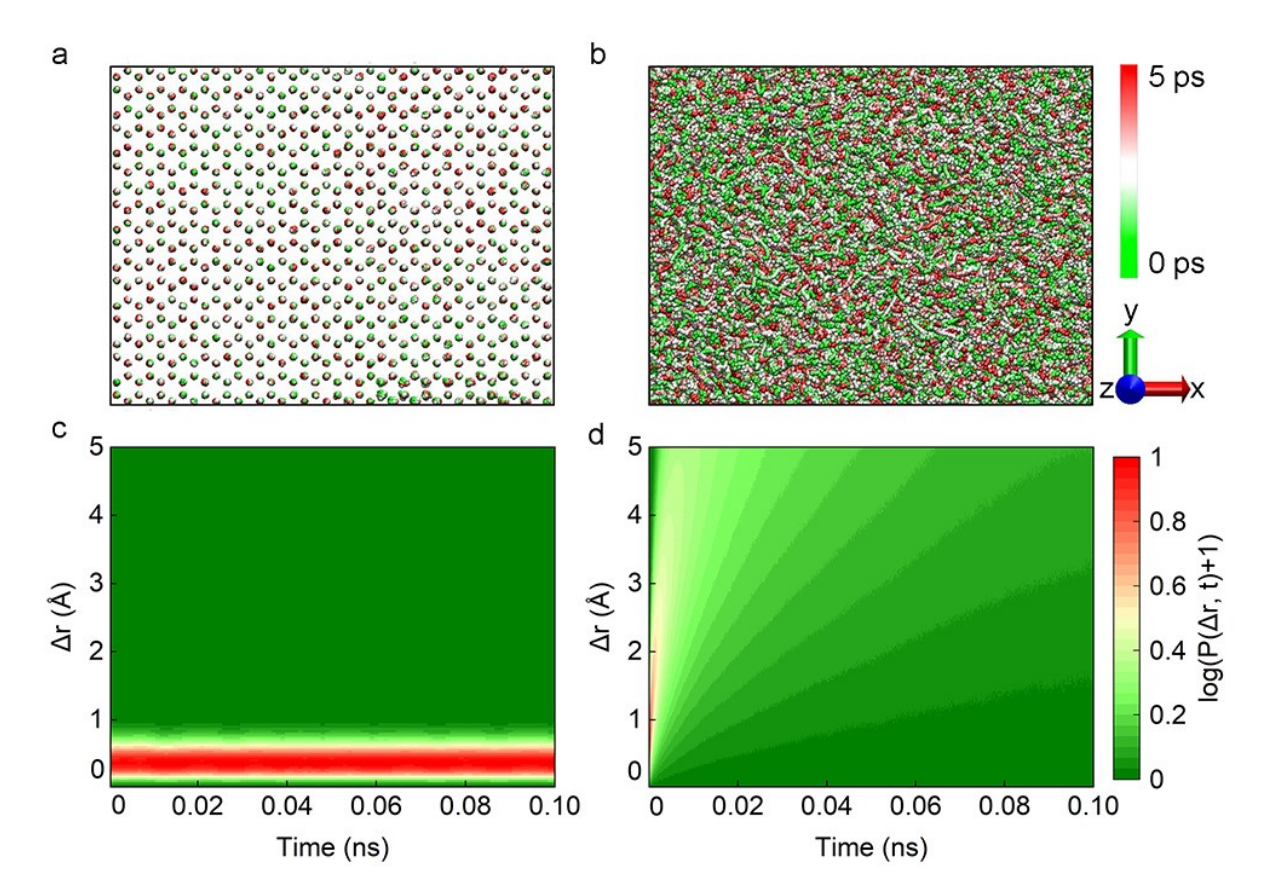


Fig. S11. Relaxed structures' snapshots of two-phase method simulations at 230 GPa and different temperatures. (a) 5000 K in ideal hcp-Fe and (b) 5500 K in full liquid iron. Self van Hove correlation functions corresponding to (c) 5000 K in ideal hcp structure and (d) 5500 K in full liquid iron. Stable Gaussian distribution in (c) indicates a typical solid behavior where atoms vibrate at equilibrium positions. Self van Hove correlation function diverges with time in (d) shows atoms diffuse disorderly in liquid iron.

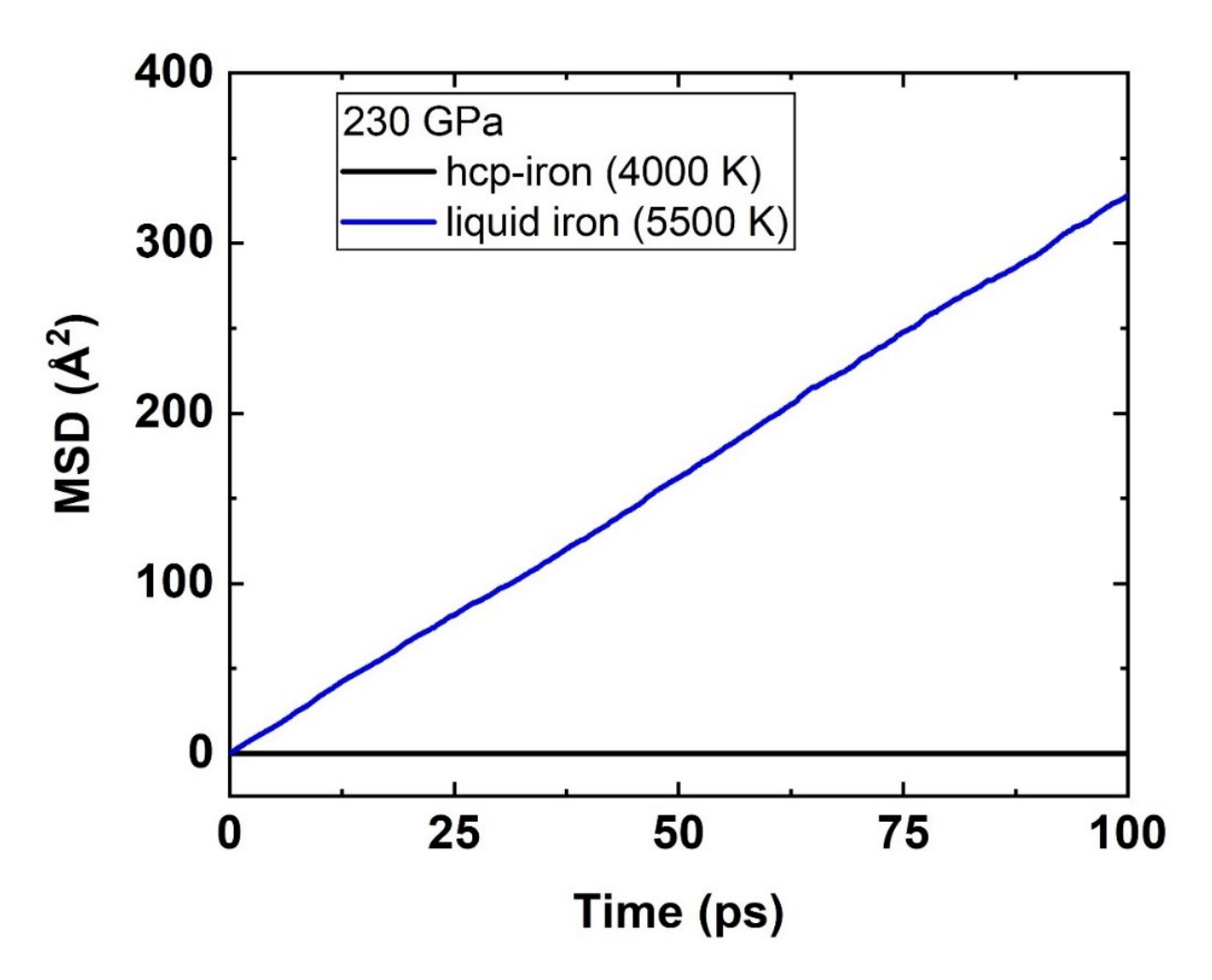


Fig. S12. Calculated mean squared displacement (MSD) of atoms in hcp and liquid iron at 230 GPa. In liquid iron, the MSD ascends steeply throughout the whole simulation time.

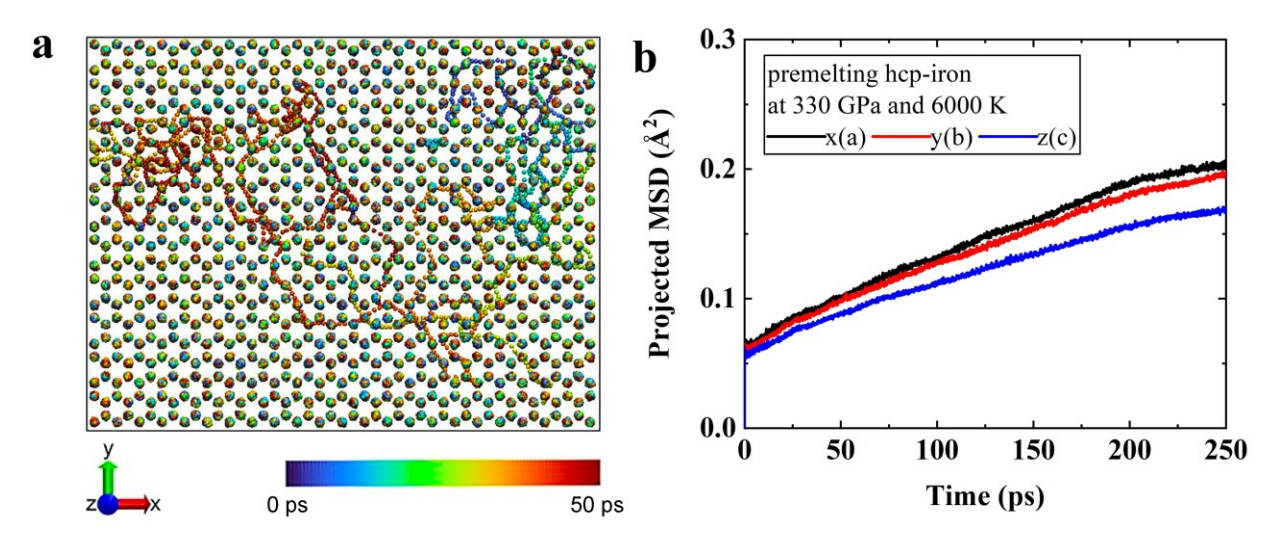


Fig. S13. Collective atomic motion of premelting hcp-Fe at the inner core conditions (~330 GPa and 6000 K). (a) Dynamical snapshots of premelting hcp-Fe at ~330 GPa and 6000 K ( $T/T_m$ ~0.97) relevant to the inner core P-T conditions. The collective motion emerges in hcp-Fe at the relevant inner-core boundary conditions. Iron atoms are colored with time progression during 50 ps. (b) Projected MSD of hcp-Fe atoms at ~330 GPa and near the melting point of 6000 K indicating the diffusivity. The diffusion is anisotropic and mostly appears in a-b (x-y) planes.

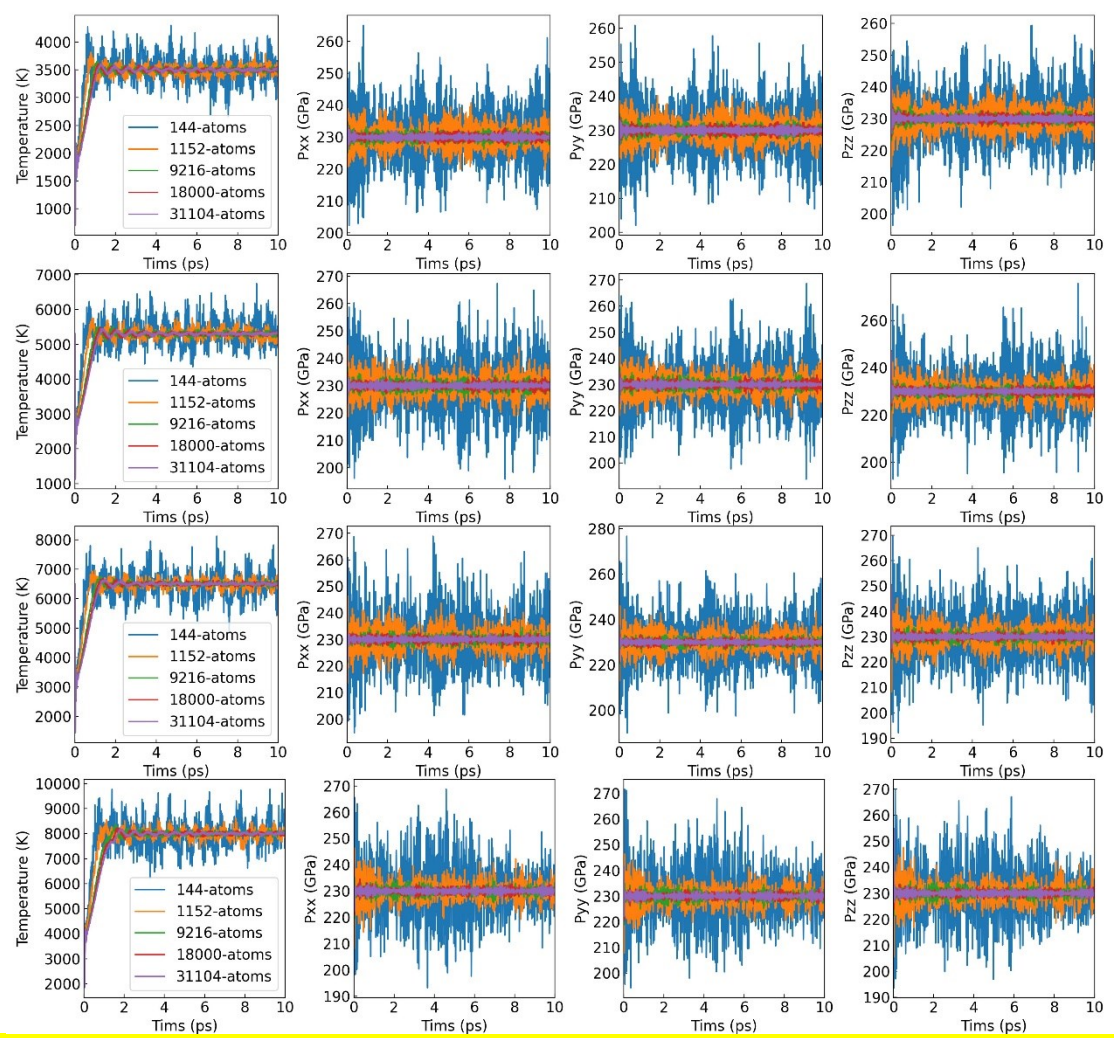


Fig. S14. Fluctuations in temperature and diagonal stress tensors of iron at 230 GPa and various temperatures using machine learning simulations with different supercell sizes. The utilized supercell configurations contained 144, 1152, 9216, 18000, and 31104 atoms, respectively. The diagonal stress tensors along the xx, yy, and zz directions were denoted as Pxx, Pyy, and Pzz, respectively. In the leftmost row, a specific temperature is represented, while the subsequent three rows indicate the three respective diagonal stress tensors (pressure) at the corresponding temperatures.

Movie S1. Diffusions of atomic collective motion of hcp-Fe at high pressure-temperature (230 GPa and  $\sim 0.98 \ T/T_m$ ). The collective motion emerges near melting in both two-phase simulations without superheating and one-phase simulations with superheating. Diffusing iron atoms are marked by red.

Table S1. Conditions of the reverse-impact experiments and the sound velocities of hcp-Fe at high pressure-temperature under shock compression.

Shot	W	Thickness	Window	$U_s$	$u_p$	$P_H$	ρ	$T_H$	$T_H/T_M$	$V_p$	$V_b$	$V_s$	$V_b/V_p$	v
No.	(km/s)	$(\delta, mm)$	materials	(km/s)	(km/s)	(GPa)	$(g cm^{-3})$	(K)	at $P_H$	(km/s)	(km/s)	(km/s)		
1	4.866(14)	1.466(2)	LiF	6.485(14)	1.616(9)	82.4(5)	10.455(8)	1600(100)	0.44(3)	8.36(17)	6.92(14)	4.06(32)	0.83(2)	0.347(21)
2	5.680(17)	1.477(2)	LiF	6.925(15)	1.895(11)	103.1(5)	10.731(9)	2090(120)	0.53(3)	8.62(18)	7.23(14)	4.06(34)	0.84(2)	0.358(20)
3	6.036(18)	1.480(2)	LiF	7.119(16)	2.018(12)	112.9(5)	10.956(10)	2330(150)	0.57(3)	8.80(19)	7.41(15)	4.11(37)	0.84(2)	0.358(21)
4	6.195(18)	1.456(2)	LiF	7.205(16)	2.072(11)	117.4(5)	11.019(10)	2450(150)	0.59(3)	8.97(20)	7.62(15)	4.10(39)	0.85(2)	0.368(20)
5	5.541(16)	0.661(1)	Al <sub>2</sub> O <sub>3</sub>	7.738(14)	2.410(10)	146.6(6)	11.401(10)	3150(200)	0.70(3)	9.52(22)	7.95(16)	4.54(41)	0.84(2)	0.358(21)
6	7.472(22)	1.682(2)	LiF	7.901(20)	2.513(15)	156.0(8)	11.511(14)	3400(200)	0.74(3)	9.72(21)	8.15(16)	4.59(40)	0.84(2)	0.358(20)
7	6.332(19)	0.734(1)	Al <sub>2</sub> O <sub>3</sub>	8.226(16)	2.719(12)	175.8(8)	11.726(12)	3840(200)	0.79(3)	9.87(19)	8.44(17)	4.43(40)	0.86(2)	0.379(18)
8	6.881(21)	0.662(1)	Al <sub>2</sub> O <sub>3</sub>	8.560(18)	2.931(13)	197.2(9)	11.937(13)	4380(250)	0.86(3)	9.86(21)	8.62(17)	4.15(46)	0.87(2)	0.389(19)
9	7.411(22)	0.662(1)	Al <sub>2</sub> O <sub>3</sub>	8.882(19)	3.135(14)	218.8(10)	12.132(14)	4920(250)	0.93(3)	9.90(22)	8.81(18)	3.91(52)	0.89(3)	0.408(19)
10*	7.673(24)	0.736(1)	Al <sub>2</sub> O <sub>3</sub>	9.040(20)	3.235(15)	229.9(10)	12.225(15)	5180(250)	0.96(3)	9.88(20)	9.10(18)	3.33(58)	0.92(3)	0.435(20)
11	7.695(23)	0.664(1)	Al <sub>2</sub> O <sub>3</sub>	9.052(19)	3.243(14)	230.8(10)	12.232(15)	5200(250)	0.96(3)	9.98(20)	9.05(18)	3.64(54)	0.91(3)	0.426(19)

Note: Eleven shots were conducted, where the pressure in iron ranges from ~82 to 231 GPa. W is the impact velocity,  $P_H$  and  $T_H$  is the shock Hugoniot pressure and temperature of iron, respectively,  $\rho$  is the density at Hugoniot pressure,  $U_s$  and  $u_p$  are the shock wave velocity and particle velocity of iron, respectively, calculated from W and the known Hugoniot relations of iron and windows,  $V_p$ ,  $V_b$ , and  $V_s$  is the longitudinal, bulk, and shear velocity of iron under shock compression, respectively. The Hugoniot relation ( $U_s = C_0 + \lambda u_p$ ) used in this study are  $U_s$  (km/s) = 3.935 + 1.578  $u_p$  with the initial density of  $\rho_0 = 7.850(2)$  g cm<sup>-3</sup> for iron (73),  $U_s$  (km/s) = 5.215 + 1.351  $u_p$  with the initial density of  $\rho_0 = 2.640(2)$  g cm<sup>-3</sup> for LiF (89),  $U_s$  (km/s) = 8.740(44) + 0.957(10)  $u_p$  with the initial density of 3.988(2) g cm<sup>-3</sup> for sapphire  $Al_2O_3$ . The parameters in parentheses are standard deviations. The used LiF and  $Al_2O_3$  crystals are <100> and <0001> orientation, respectively. The sapphire is denser than that of LiF crystal. Therefore, iron impacting onto sapphire can generate much higher pressures than that by LiF. \*In shot No. 10, only the longitudinal sound velocity was measured, the bulk and shear sound velocity were estimated from the thermodynamic calculations.